Vol 125, pp 1465-1488

The Influence of Mesoscale Orography on a Coastal Jet and Rainband

James D. Doyle

Marine Meteorology Division
Naval Research Laboratory
7 Grace Hopper Ave.
Monterey, CA 93943-5502

24 October 1996

Submitted For Publication In *Monthly Weather Review*

Revised Manuscript

DISTRIBUTION STATEMENT A
Approved for public release;
Distribution Unlimited

Corresponding Address: 1 April-31 December 1996
James D. Doyle
European Center for Medium Range Forecasting
Shinfield Park
Reading, Berkshire RG2 9AX, United Kingdom

DTIC QUALITY INSPECTED 8

19971027 059

ABSTRACT

The role of mesoscale orography along the central California coast in the development and evolution of a coastal jet and rainband is investigated using a high-resolution, triply-nested, nonhydrostatic numerical model. Comparison of the model simulations, which use horizontal grid increments of 5 km and 2 km on the inner-computational meshes, with a coastal mesoscale observation network indicates that the fine-scale structure of the jet and rainband dynamics are adequately simulated, although phase and orientation errors occur. The observed and simulated near-surface winds have maximum speeds that exceed 22 m s^{-1} and a direction nearly parallel to the coastline and topography.

Force balance analysis indicates that blocking in the lowest 500 m and flow over the coastal range above this layer contribute to mesoscale pressure perturbations, including pressure ridging upstream of the coastal mountains, which force the ageostrophic dynamics of the coastal jet. Pressure perturbations associated with the topographic flows induce a complex mesoscale response that adds rich mesoscale structure to the jet including a wake region that forms on the lee side of the coastal range that limits the horizontal scale of the jet. Sensitivity test results underscore the multi-process character of the coastal dynamics, and the importance of the coastal topography and differential frictional drag at the land/sea interface for the formation and amplification of the jet. The mesoscale response to steep coastal topography results in a 45% enhancement to the near-surface jet strength. The onshore movement of line convection at the leading edge of a weak front is impeded by steep coastal topography in both the radar observations and numerical simulations. Low-level blocking forces the rainband to emulate a wedge-shaped structure with a coastal jet that is dynamically trapped between the steep coastal topography and the front.

1. INTRODUCTION

The complex forcing that frequently is present in the coastal zone can significantly modulate the evolution of mesoscale phenomena, such as fronts (e.g., Steenburgh and Mass 1996) and lower-tropospheric wind maxima embedded within synoptic-scale disturbances (e.g., Doyle and Warner 1993; Overland and Bond 1995; Colle and Mass 1996). This local forcing may result from an amalgamation of intense gradients in heat, moisture and momentum transport that occur at the land/sea interface. Steep coastal mountain ranges further add to the complexity of the forcing (e.g., Reed 1980; Overland 1984; Mass and Ferber 1990; Overland and Bond 1993). Numerous recent studies have contributed to a rapid advance in the understanding of the heterogeneous character of the coastal zone processes by addressing individual local forcing mechanisms (Rotunno et al., 1992; Rogers 1995). Nevertheless, there are still many outstanding questions pertaining to the multi-process and multi-scale nature of mesoscale forcing in littoral regions.

The impact of orography upon airflow and precipitation has been extensively investigated (e.g., Smith 1979; Smith 1989). Numerous theoretical and numerical studies have documented the relationship between the airflow response to topographic effects and the nondimensional parameters: Nh/U and the Rossby number (R_0=U/fL), where N is the buoyancy frequency, h is the height of the mountain, U is the speed of the free airstream, f is the Coriolis parameter and L is the mountain half-width scale. In the nonrotating limit, Pierrehumbert and Wyman (1985) found Nh/U to be the sole parameter characterizing the upstream response to flow around an obstacle. Low-level flow can be blocked by an obstacle when Nh/U > 1 (Smith 1979), which may result in downstream vortex shedding (Smolarkiewicz et al. 1988; Smolarkiewicz and Rotunno 1989, 1990) and upstream deceleration (Pierrehumbert 1984; Pierrehumbert and Wyman 1985). Along the west coast of the United States, orographically induced blocking commonly occurs (Neiburger 1960) and can result in particularly complex mesoscale responses in the coastal zone (e.g., Overland and Bond 1993, Holt 1996). For large Nh/U, flow stagnation may be present on the upwind and

lee sides with lateral deflection persisting downstream to form a wake region (Smith 1980; Smith and Smith 1995).

In the rotating case, the Nh/U and R_o can be used to describe the parameter space of the atmospheric response to flow impinging upon mesoscale mountains (e.g., Pierrehumbert and Wyman 1985; Trüb and Davies 1995). For blocked flow in the rotating case, the maximum extent of the deceleration region upstream of an obstacle is of the order of the Rossby deformation radius (L_R = Nh/f) (Pierrehumbert and Wyman 1985). For typical mesoscale mountain ranges, the flow characteristics lie in the intermediate parameter space of R_o and Nh/U. Trüb and Davies (1995) found for this intermediate parameter range, as R_o decreases, the flow response changes from vertically propagating waves (R_o>1), to a leeward wavetrain of near inertial waves (R_o~1), and finally transitioning to a state dominated by the adjustment process associated with scale contraction (R_o<1). In terms of relevant scaling parameters, steep coastal topography can be expressed as the condition when the Burger number (B=hN/fL) exceeds unity (Pierrehumbert 1984; Pierrehumbert and Wyman 1985). For mesoscale mountains (L << U/f) such as the coastal range of California, the maximum mountain height primarily determines the character of the barrier effects, while the steepness is important for atmospheric response to broad mountains (L~O(U/f)) (Pierrehumbert 1984).

Lower-tropospheric wind maxima are often observed in the coastal zone and can be enhanced by coastal orography due to cold-air damming effects, such as barrier jets (e.g., Bell and Bosart 1988; Doyle and Warner 1993) and low-level blocking due to onshore flow characterized by a large Nh/U regime (e.g., Pierrehumbert and Wyman 1985; Overland and Bond 1993, 1995). The summertime northerly near-surface jet along the California coast can be enhanced by the coastal ranges as a result of blocking of the onshore flow (Holt 1996), modulation of the diurnal heating cycle and coastal baroclinicity, and generation of intertia-gravity waves associated with offshore across-ridge flow (Burk and Thompson 1996). Mass and Ferber (1990) discuss the development of ridging upwind of the Olympic Mountain Range along the coast of western Washington state before a cold frontal passage. An along-shore

gradient of the orographically-induced pressure perturbation becomes superimposed upon the synoptic-scale pressure field, which results in a low-level enhancement of the along-shore winds associated with the prefrontal lower-tropospheric wind maximum. Often, these wind maxima are manifested as supergeostrophic flows parallel to the local topography (Overland and Bond 1993). In these cases, the balanced response to blocked onshore flow will grow horizontally offshore from the coastal mountains to a limit given by L_R (Pierrehumbert and Wyman 1985).

The mesoscale characteristics of fronts associated with extratropical cyclones may be altered substantially by blocking and topographic deformation associated with steep coastal orography. Bjerknes and Solberg (1921) described the low-level blocking of a warm frontal zone that results in topographic deformation and precludes the lower portion of the front from passing the complex coastal topography of Norway. Davies (1984) deduced an analytical solution for a front moving over topography and showed that, in the semi-geostrophic limit, the character of the flow governing the topographic retardation of a cold front in neutral stratification is determined a rotational Froude number and a front-mountain aspect ratio. Numerous other studies indicate that fronts have a tendency to weaken on the windward side of mountains and strengthen again on the lee slopes (e.g., Zhender and Bannon 1988; Williams et al. 1992). Observational studies have documented the marked deformation effects of orography upon fronts that include blocking and splitting of low-level air flow, gravity wave generation and foehn-type flows (e.g., Hoinka and Smith 1988; Kurz 1990; Volkert et al. 1991; Hoinka and Volkert 1992). Schumann (1987) found that the movement of the lower portion of a front will be impeded by mesoscale topography when Nh/U is large, the front is shallow, a large temperature difference exists between the warm and cold air, the front-normal velocity is small, and the mean-state stratification is large. Additionally, high and steep mountains result in the largest obstruction to frontal movement.

The coastal range of central California is one such region where the juxtaposition of the steep coastal orography, moist marine layer and differential flux forcing can significantly

modulate the coastal mesoscale environment. The coastal range of central California is comprised of five distinct mountain ranges (Fig. 1). The Santa Lucia Mountains are located along the coast to the south of the Monterey Peninsula. The Salinas River Valley separates the Sierra de Salinas from the Gabilan and Diablo Ranges to the east, with the Carmel River Valley located between the Sierra de Salinas and Santa Lucia Ranges. Several regions in these ranges have elevations in excess of 1000 m. The Santa Cruz Mountains are located along the northern portion of the Monterey Bay. The coastline to the south of Monterey is a particularly interesting region to examine the role of orographic modulation of coastal phenomena because of the marked steepness of the coastal range, the proximity of the peaks to the coast, and the near linear-structure of the ridge. The coastal range in this region is mesoscale in character with cross mountain widths of ~50 km.

During early January 1995, a major extratropical cyclone and attendant frontal system impacted the central California coast with damaging winds and heavy precipitation in the coastal mountains. This weather system was one of a series of cyclones that saturated the soil, filled local reservoirs to capacity, caused local flash floods and eventually resulted in widespread catastrophic flooding several months later. Additionally, the mesoscale forcing associated with this weather system resulted in wind damage to trees and homes on the Monterey Peninsula. The operational numerical guidance and forecasts were not adequate in this case and did not alert the general public of the potential for severe coastal winds. Although some of the local meteorology was relatively extreme, the nature of the orographic modulation of the front and lower-tropospheric winds is a common characteristic for the central California coast and for coastal regions in general.

There have been numerous investigations of cyclone and frontal interactions with topography. However, the modulation of mesoscale forcing associated with frontal zones by steep topography in the presence of coastal processes is still not well understood. In this study, the interactions of an intense mesoscale precipitation system and a strong prefrontal low-level jet (LLJ) with the coastal-zone environment and coastal orography is studied using the Navy's

high-resolution, nonhydrostatic mesoscale modelling system in a pre-operational test mode. The specific objectives of this study are to: 1) examine the structure of the prefrontal lower-tropospheric winds during the landfall stage in a region of complex coastal orography, 2) explore the interactions of the coastal zone forcing with the frontal precipitation, and 3) evaluate the ability of a sophisticated nonhydrostatic mesoscale model to predict the mesoscale structures associated with the complex coastal zone forcing in a mode that emulates a next-generation operational configuration. The numerical model used in this study is described in section 2. The synoptic-scale conditions are presented in section 3. The results are described in section 4 and discussion of the implication of the results is presented in section 5. The summary and conclusions of this study appear in section 6.

2. MODEL DESCRIPTION

The atmospheric portion of the Navy's Coupled Ocean-Atmospheric Mesoscale Prediction System (COAMPS) (Hodur 1993) is used in this study. The triply nested, three-dimensional model solves the nonhydrostatic, fully compressible equations of motion and makes use of a terrain following sigma coordinate system, σ_z, following Gal-Chen and Somerville (1975). Physical parameterizations include short- and long-wave radiation parameterization (Harshvardhan et al. 1987), a level 2.5 subgrid-scale planetary boundary-layer parameterization with a predicted turbulent kinetic energy (TKE) budget (Therry and LaCarrére 1983), and a convective parameterization scheme (Kain and Fritsch 1990). Explicit budget equations for cloud water, cloud ice, rain drops, snow flakes, and water vapor are used to predict the evolution of the moist processes (Rutledge and Hobbs 1983).

The nonhydrostatic model initial fields are created from multivariate optimum interpolation analyses of surface, upper-air sounding, aircraft and satellite data that are quality controlled (Baker 1992) and blended with 1° resolution first-guess fields from the Navy Operational Global Analysis and Prediction System (NOGAPS, Hogan et al. 1991) following Barker (1992). The initialization time is 1200 UTC 6 January 1995. Real-data boundary conditions make use of NOGAPS *forecast* fields. Thus, the COAMPS prediction system applied in this

manner mimics a real-time forecast situation. The topographic data are based on the State Defense Mapping Agency's 100-m resolution data set. The terrain data for the second (Δx=6 km) and third (inner-most; Δx=2 km) grid meshes, shown in Figs. 2a and 2b, respectively, indicates that the local topographic features associated with the coastal range are well represented.

The control simulation has a domain defined by a grid of 133x133 points for the coarse mesh, and medium and fine mesh grids of 166x166 points. The horizontal resolution is 18 km, 6 km, and 2 km for the coarse-, medium- and fine-mesh grids, respectively. The model top is at 30 km with 30 irregularly spaced vertical levels and 14 levels in the lowest 1.5 km to sufficiently resolve the boundary-layer processes. Sensitivity tests were performed with a slightly degraded resolution because of computational expense. Horizontal grid increments of 45 km, 15 km, and 5 km were used for the coarse-, medium- and fine-mesh grids, respectively, with 30 vertical levels for the sensitivity experiments.

3. SYNOPTIC-SCALE CONDITIONS

At the model initialization time, 1200 UTC 6 January 1995 (06/12), the COAMPS synoptic-scale analyses indicate that a large-scale developing cyclone with a central pressure of 984 mb was positioned approximately 1000 km to the west of the northern California coast (Fig. 3a). The 850-mb thermal gradient (Fig. 4a) associated with the warm and occluded fronts is considerably stronger than the gradient along the primary and secondary cold frontal boundaries. Low-level wind speeds in excess of 25 m s^{-1} were located along the baroclinic zone to the rear of the primary cold front (Fig. 4a). Aloft, a strong subtropical jet stream was positioned along the southern portion of an amplifying 500-mb trough at this time with a wind-speed maximum at 300 mb in excess of 70 m s^{-1} as shown in Fig. 5a.

A sea-level pressure analysis for 07/00, shown in Fig. 3b, indicates that the central pressure deepened by 12 mb in the previous 12-h and an 80-m decrease occurred in the 500-mb geopotential height minimum in the trough (Fig. 5b). The 07/00 infrared satellite imagery (Fig. 6) indicates a comma cloud shield that is consistent with a mature baroclinic cyclone

with a broad precipitation shield ahead of the cold front. An intense subtropical jet stream contains a local wind-speed maximum of over 65 m s^{-1} to the south of the 500-mb vorticity maximum near the base of the trough (Fig. 5b). A corridor of strong low-level winds was positioned to the east of the cold front and to the north of the occluded front (Fig. 4b). Several ship observations at 07/00 reported surface wind speeds in excess of 20 m s^{-1} ahead of the surface cold front and to the north of the occlusion (Fig. 3b). The thermal gradient associated with the cold front was generally weak at low-levels (Fig. 4b), which may have resulted from the frontolytic effects of boundary-layer heat fluxes on the cold side of the front. During the following 6-h period, the cold-frontal boundary and associated southerly LLJ propagated rapidly eastward at ~20 m s^{-1}, and moved ahead of the upper-level support. The sparse nature of offshore observations may contribute to analysis uncertainties in defining the offshore mesoscale structures. Although this frontal boundary was decaying as it made landfall, the prefrontal mesoscale low-level wind maximum was enhanced by steep coastal topography and subsequently resulted in the severe coastal winds.

4. RESULTS

a. Control Simulation Results

1) UPSTREAM FRONTAL AND COASTAL JET STRUCTURE

The evolution of the lower-tropospheric wind maximum and associated weakening front is depicted by the model-simulated 900-mb equivalent potential temperature (θ_e) and wind field for the second grid mesh (Δx=6 km), shown in Figs. 7 and 8, respectively. At the 6-h simulation time (06/18), a weak and diffuse baroclinic zone is present along the coast with colder temperatures near the coast (Fig. 7a), perhaps a remnant of the weakening southern extension of the warm frontal zone. The cold front is located further to the west at this time, outside of the second mesh domain. An offshore lower-tropospheric wind maximum (Fig. 8a) in excess of 30 m s^{-1} is present at this time ~200 km to the west of the California coast embedded in the eastern portion of a broad band of precipitation.

A vertical cross section for the second grid mesh (Δx=6 km) of model-simulated poten-

tial temperature, mountain normal and parallel wind components, oriented normal to the Santa Lucia Range and constructed along the A-A' axis (cross section location is shown in Fig. 2a) for the 6-h time (06/18) are shown in Figs. 9a, 10a and 11a, respectively. Prior to the approach of the front, the lower-tropospheric isentropes (Fig. 9a) are quasi-horizontal offshore with enhanced stability capping the marine layer. A cold dome is positioned just to the west of the topography and represents a balanced response to the blocked onshore flow as evident in the mountain-normal component in Fig. 10a (Pierrhumbert and Wymann 1985). A layer of significant vertical shear is present in the mountain-normal component as a result of the upstream deceleration of the flow, consistent with the theoretical results of Pierrehumbert and Wyman (1985). A small mountain-normal component, directed offshore near the coastal mountains, is an artefact of the cross section plane orientation that is not precisely normal to the low-level flow at this time and location. The mountain-parallel component (Fig. 11a) shows a low-level wind speed maximum of nearly 24 m s^{-1} positioned at 970-mb level and ~200 km offshore. This offshore position may result from the combined forcing of the low-level blocking by the coastal range and the frontal forcing.

Nondimensional parameters are diagnosed from the model simulation performed without topography. At this time, the undisturbed flow normal to the coastal range in a layer from the surface to mountain top is ~7-9 m s^{-1} and N is ~1.7×10^{-2} s^{-1}, which yields Nh/U ~1.9-2.4, R_o~ 1.75-2.25, and B~3.3-5.4. This implies that the parameters associated with the flow near the steep coastal topography lay in the nonlinear regime. For these parameters, Trüb and Davies (1995) found wave energy source to be vertically propagating gravity waves, which is consistent with Fig. 9a, although the gravity waves are weak at this time and in this cross section plane. Additionally, the results of Pierrehumbert and Wyman (1985) suggest that the blocking of low-level flow and topographic influences upstream of the coastal range should be present at this time for these nondimensional parameters. In this case, the blocking is maintained by the wind component normal to the coastal mountains as opposed to the total wind velocity.

In the following 6-h period, the weak baroclinc zone associated with the cold front is

apparent in the 900-mb θ_e field (Fig. 7b). The model erroneously moves the front eastward too rapidly, with a ~150 km position error by the 12-h time (07/00) relative to the estimated observed position (Fig. 3b). At the 12-h time (07/00), the thermal difference across the front is only 2 K at 900-mb, which is not atypical for marine fronts (e.g., Bond and Shapiro 1991) particularly at this latitude. The vertical cross section of potential temperature for the 12-h time (07/00) (Fig. 9b) constructed along a plane oriented normal to the coast, suggests that the sloping baroclinic zone persists offshore, immediately upstream of the coastal mountains, as a manifestation of the response to low-level blocking. The blocked characteristics of the flow is consistent with a Nh/U~0.9-1.2, which is sufficiently large for upstream influences to be present (Pierrehumbert and Wyman 1985). The thermal signature of the offshore frontal zone in this cross section plane is very weak. Weak signatures of vertically propagating gravity waves are apparent just downstream of the peaks of the coast range. Results from the third grid mesh (Δx=2 km) discussed in the following section indicate that larger amplitude vertically propagating gravity waves exist in the plane parallel to the Santa Lucia Range in the vicinity of Monterey Bay (Fig. 15) associated with this along-ridge flow above the blocked layer. The flow parallel to the coastal range near mountain top has increased substantially over the previous 6-h period to greater than 20 m s^{-1} (Fig. 10b).

A significant speed shear is present along the front at 12 h (07/00) with a well defined lower-tropospheric wind speed maximum in excess of 35 m s^{-1} present ahead of the front ~100 km offshore (Fig. 8b). A second local wind speed maximum is located along the coast in the lee of the Santa Cruz Range. A distinct cyclonic shear zone is present at the leading edge of the front with southerly wind directions ahead of the front, which are more parallel to the coastal topography than farther offshore. This coast-parallel direction results from the balanced response to partial low-level blocking by the coastal topography, in spite of the 900-mb surface being near the top of the coastal topography. The fine-scale results from the third-grid mesh, discussed in the following section, indicate partial blocking of the near-surface flow. At this time, intense cross-mountain flow persists above the blocked layer (Fig. 10b),

with the mountain-normal wind speed of nearly 30 m s^{-1} at 900 mb offshore upstream of the blocked region. The coast-parallel wind component (Fig. 11b) has transitioned over the 6-h period from 06/18-07/00 from a frontal jet located ~150 km offshore to a low-level wind speed maximum of 28 m s^{-1} positioned just offshore of the steeply sloping coastal mountains nearly 500 m above the surface or midway to the mountain top. Additionally, during the 6-h period the along-ridge flow has more than doubled to over 20 m s^{-1} near the coastal range top. It is noteworthy that the low-level flow perturbation due to blocking present in the cross-mountain flow decays away from the coastal range approximately five times more rapidly than the mountain-parallel flow. This is in general agreement with the results of Pierrehumbert (1984), who found that upstream perturbation in the along-mountain flow decays as x^{-1}, while the cross-mountain flow perturbation decays as x^{-2}. Additionally, the decrease with height of the along-mountain flow above the boundary layer and increase with height of the cross-mountain component are consistent with the results of Pierrehumbert (1984) and Pierrehumbert and Wyman (1985) for blocked low-level flow upstream of mesoscale mountains. The consequence of this shear is that is significant cross-ridge component is present above the blocked layer.

The front intensifies offshore and becomes horizontally deformed by the coastal topography between the 12-h and 18-h times (Fig. 7c). The frontal thermal and shear gradients become quite diffuse onshore, in part as a result of flow interactions with the complex coastal topography. The low-level jet remains most intense ahead of the front and has become wedged between the front and the coastal topography (Fig. 8c). The flow has a significant component onshore at this level, especially just to the south of the Monterey Bay to the rear of the front.

A vertical cross section for the second grid mesh (Δx=6 km) of model-simulated potential temperature oriented normal to the coast south of the Santa Lucia Range and constructed along the B-B' axis (cross section location is shown in Fig. 2a), which is to the south of axis A-A', for the 18-h time (007/06) is shown in Fig. 9c. The front is located nearly 150 km

offshore of the coastal mountains and has the strongest horizontal thermal gradient in the 950-800 mb layer. The steep coastal topography, relatively large static stability, and the shallow depth of the front are conducive for topographic modulation of the front in agreement with the idealized studies of Davies (1984) and Schumann (1987). A sloping baroclinic surface associated with the blocking is present between the front and coastal mountains, consistent with the strong coast-parallel jet (Fig. 11c) located along the sloping topography. A distinct cyclonic shear zone exists in the coast parallel component along the frontal zone with a local wind speed maximum to the rear of the front near 800 mb. The coast-normal wind component is once again indicative of blocked of onshore flow (Fig. 10c). In the post-frontal boundary layer, the stability is considerably weaker compared to the pre-frontal boundary layer (Fig. 9c). As a result, Nh/U is considerable smaller behind the front (~0.55) and the postfrontal winds have transitioned to a regime characterized by unblocked onshore flow (Fig. 8c).

2) FINESCALE SIMULATION OF LOWER-TROPOSPHERIC WIND FIELD

As the frontal system approached the central coast of California, the interaction of the LLJ with the complex coastal orography becomes more apparent. The evolution of the 5-m winds for the third grid mesh is shown in Figs. 12a-d for the 6-h (06/18), 9-h (06/21), 12-h (07/00), and 15-h (07/03) simulation times, respectively. The wind speeds are relatively weak in the Monterey Bay region at 6-h (06/18) with some indication of blocking of the southerly flow, flow splitting around the Santa Lucia Range to the south, and channelling through the Salinas River Valley consistent with the relatively large Nh/U (~1.9-2.4). As a result of the flow splitting, a weak wind speed region is established near the Monterey Peninsula in the lee of the Santa Lucia Range. In general, the surface wind observations, shown in Fig. 12a, are in good agreement with the model-simulated 5-m winds. At this time, the largest near-surface winds are located near the western boundary.

The simulated 5-m wind speeds increase markedly along the coast in the following 3 hours (Fig. 12b). A large area of wind speed greater than 15 m s^{-1} exists along the coast with local maxima just offshore of the Santa Lucia Range and to the southwest of San Francisco

Bay. This model increase in low-level wind speed of ~5 m s^{-1} near Monterey Bay appears to be excessive when compared with the buoy observation. The simulated wind-speed minimum or wake in the lee of the Santa Lucia Range associated with the flow splitting extends across the Monterey Bay and has narrowed somewhat in the cross-wake direction over the last 3 h, concurrent with the increased cross-mountain component and decreased Nh/U.

At the 12-h time (07/00), the simulated 5-m wind direction (Fig. 12c) has veered slightly in the coastal zone in agreement with the surface observations (e.g. evident in the San Francisco buoy observation), although the model has a 30° wind direction error relative to the Monterey Bay buoy observation. The wind speeds have increased by 5-10 m s^{-1} over the previous 3-h period just offshore of the coast between San Francisco Bay and the region south of Monterey Bay, in general agreement with the observations. The buoy observations to the west of the Monterey and San Francisco Bays both indicate wind speeds of 15 m s^{-1}. The maximum simulated wind speeds are located along the coastline near the Monterey Peninsula suggesting that orographic and coastal forcing may be acting in concert to produce the low-level wind maximum. It is noteworthy that the weak wind speed region in the lee of the Santa Lucia Range is less apparent than at the 6-h and 9-h times (Figs. 12a-b) because of a decrease in Nh/U as a result of a marked increase in the cross-mountain flow of over 15 m s^{-1} during this time period (e.g., Fig. 10b). The offshore near-surface flow at this time has become nearly parallel to the coastal topography as a consequence of the blocked low-level flow, consistent with the results of Pierrehumbert (1984) and Pierrehumbert and Wyman (1985) for an upstream Nh/U of approximately 0.9-1.2 at this time. At the 900-mb level, which is near the top of the Santa Lucia Range, the flow has a greater across-ridge component than the 5-m air flow (Fig. 8b). However, even near the mountain peaks, evidence of flow deflection around the coastal orography is apparent.

The simulated 5-m winds at the 15-h time (07/03), shown in Fig. 12d, indicates that the wind-speed maxima remain along the coastline; specifically one maximum is in excess of 20 m s^{-1} just to the south of the Monterey Bay along the steep coastal topography. A narrow

wind-speed minimum extends diagonally across the Monterey Bay as a result of flow splitting in the lee of the Santa Lucia and Sierra de Salinas Ranges. Surface observations just to the south of Moss Landing, at the Naval Postgraduate School's 915 MHz wind profiler site, indicate wind speeds of 10-12 m s^{-1}, which support the dual wind speed maximum in the Monterey Bay. The weak frontal boundary is apparent in the wind shear zone approximately 100 km offshore. A great deal of fine-scale structure is now evident onshore in the near-surface winds including regions of low-level channelling of flow.

A subsection of the 5-m winds for the 2-km resolution fine mesh for 13-h (07/01) is shown in Fig. 13. A wake, which is meridionally oriented across the Monterey Bay, appears to have its origin in the flow splitting around the Sierra de Salinas and Santa Lucia Ranges (Fig. 13a). This weak wind speed region is rather shallow with little discernible signature at the 900-mb level (Fig. 8b). Simulated wind speeds are over 50% weaker in the wake than in the LLJ maximum positioned near the coast, south of the Monterey Peninsula. The model-simulated wind speeds are in general agreement with the observations plotted in Fig. 13a, although a directional error of ~30° is present in the vicinity of the M2 buoy. For example, a special observing site at Granite Canyon (GC), which is located near the model-simulated surface wind speed maximum, reported a wind speed of 18 m s^{-1} at 07/01. Peak wind speeds were in excess of 24 m s^{-1} several hours later. Weak winds are present near the northern portion of the Monterey Bay in agreement with the observation at the University of California-Santa Cruz (UC). Three observations from Monterey Bay Research Institute's buoys M1 and M2, and Pacific Gas and Electric's Moss Landing site (ML) clearly indicate the presence of a wind-speed minimum near the center of the bay consistent with a wake feature. The M1 buoy has wind speeds at this time 5 m s^{-1} less than the Moss Landing site and 8 m s^{-1} less than the offshore buoys M2 and 46042. A time series of observed surface wind speeds from these three sites is shown in Fig. 14. The surface wind-speed minimum in the center of the bay is a persistent mesoscale feature for the time period prior to frontal passage. At times, the observed winds at M2 and Moss Landing are over 10 m s^{-1} stronger than at M1.

The simulated winds are too strong in the wake region relative to the M1 buoy observations. After the observed frontal passage (~07/05) and the flow becomes unblocked in the postfrontal airmass, the wind speed increases at buoy M1 and decreases at Moss Landing.

The low-level confluence located across the Monterey Bay associated with the flow splitting is apparent in the observations as well (Fig. 13b). Observations from the M1 buoy indicate a greater easterly component than the Moss Landing site, M2 and 46042 buoys suggesting near-surface confluence west of M1. The simulated streamlines clearly show the presence of the near-surface flow splitting around the Sierra de Salinas and Santa Lucia Ranges. It is noteworthy that even in the presence of some flow splitting around the coastal ranges, a substantial amount of flow ascends and descends the coastal ridges yielding a partially blocked mesoscale environment.

A vertical cross section of potential temperature constructed along a plane parallel to the Santa Lucia Range along the axis of the low-level wake region (line C-C' in Fig. 2b) for the 13-h time (07/01) is shown in Fig. 15. Because of significant wind velocity shear below the mountain top, the cross section orientation is nearly parallel to the flow near the top of the coastal mountain peaks at this time (Fig. 11b). The topographically unmodulated flow has a strong cross-mountain component at low-levels and a greater along-mountain component near the mountain ridge peak. The wake in the vicinity of the Monterey Bay (Fig. 13a) is confined below 975 mb and downstream of the gravity waves in the lee of the coastal mountains. The shaded regions of large TKE values in Fig. 15 indicate that the wake region was most likely associated flow splitting rather than with breaking vertically propagating gravity waves. This result is consistent with the proposed regime diagram for hydrostatic wave breaking and flow splitting (Smith 1989) for $Nh/U \sim 1.5$ and an aspect ratio (mountain width to length) of ~0.6. The vertically propagating gravity waves are also consistent with the idealized modelling study of Trüb and Davies (1995) for the scaling parameters $R_o \sim 3\text{-}4$ and $Nh/U \sim 0.9\text{-}1.2$.

The winds derived from the Naval Postgraduate School's 915 MHz profiler located at the Fort Ord site (location FO in Fig. 13a) between 06/12 and 07/12 are shown in Fig. 16a. Spo-

radic areas of missing winds due to falling precipitation were replaced by interpolation. An intense southerly jet in excess of 25 m s^{-1} is clearly evident between 1000 and 1500 m between 07/04 and 07/08. Little evidence of the passage of the weak frontal zone, other than the strong cyclonic shear zone to the rear of the low-level wind speed maximum, is found at this site. The maximum wind speed at 100 m above the surface is in excess of 22 m s^{-1}. The 2-km grid-increment mesh simulated time series of winds interpolated to the profiler site is shown in Fig. 16b. The model captures the general structure of the jet; however, the speeds are 5-10 m s^{-1} too strong above 975 mb (~300 m). The model also has somewhat stronger veering in the low-level winds than observed. Additionally, the maximum wind speeds near the surface associated with the coastal jet occur 1-3 h sooner than observed for this site. Recognizing the difficulties associated with verification at a single profiler site, the model captures the temporal wind profile changes with reasonably skill.

3) SIMULATION OF PRECIPITATION STRUCTURES

Copious precipitation was associated with the landfall of the cold-frontal boundary despite the weak thermal structure. The 24-h observed precipitation data based on the 1200 UTC 6 January - 1200 UTC 7 January time period, shown in Fig. 17a, is rich with mesoscale structure that is well correlated with the local topography. These precipitation data are based on a mesonetwork of observations maintained by the Monterey County Water Resources Agency. Along the Santa Lucia Range, observed 24-h precipitation totals are in excess of 75 mm. Marked precipitation gradients exist along the lee side of the Santa Lucia Range, which is in agreement with studies that have shown a general decrease of precipitation with elevation in isolated valleys (e.g., Longley 1975). These windward and lee-side effects are consistent with the strong cross-mountain flow near the top of the coastal range. The existence of significant windward enhancement and leeward rain shadows for other mountain ranges are well documented. For example, Mass and Ferber (1990) note that the mean annual precipitation on the windward slopes of the Olympic Mountains is an order of magnitude larger than the leeward portions. In this case, to the north of the coastal range at the mouth of the Salinas River

Valley, precipitation amounts are an order of magnitude less than in the coastal mountains.

The model-simulated 24-h accumulated precipitation for the same period of time is shown in Fig. 17b. The precipitation amounts appear to be correlated with the steepest slopes of the mountains. The maxima are located near the mountain peaks immediately along the coast in contrast to the often observed precipitation maximum found in other regions along the windward slopes well below the peak, such as for the mountains of southern and central Norway (Nordø and Hjortnæs 1966) . The resolution of the rainguage network is not sufficient to identify the precise location of the observed maxima along the coastal mountain slopes. An offshore secondary maximum extends from the highest topography to the southwest as a result of line convection associated with the frontal zone becoming nearly stationary due to topographical forcing discussed below. The model appears to over predict the precipitation along the Santa Lucia Highlands and produces excessive precipitation along the lee slopes and to the north of the range. Nevertheless, the orographic enhancement and lee-side minima associated with the topography appear to be simulated quite realistically, especially considering the known difficulties in quantitatively verifying precipitation using rainguages. Additionally, lack of model initialization data upstream over the eastern Pacific is likely deleterious to the moisture initialization.

As the decaying frontal boundary moved rapidly eastward toward the coast, a convective line similar to a narrow cold-frontal rainband (e.g., Hobbs and Persson 1982) was positioned at the frontal boundary. Data from the National Weather Service WSR-88D Doppler radar, located in the Santa Cruz Mountains, indicated that a band of reflectivity values greater than 50 dBZ was located approximately 40 km offshore embedded within a larger region of precipitation at 07/06 (Fig. 18a). Weaker echo regions were apparent immediately behind the band. As this convective line approached the steep coastal topography to the south of Monterey, the topography substantially influenced the rainband characteristics. For example, the WSR-88D radar data for 0653 UTC 7 January (Fig. 18b) indicates that the coastal topography appears to influence the movement of the line convection at the leading edge of the front that results in

the transition from a near-linear feature offshore to a somewhat deformed wedge-shaped convective line offshore of the Santa Lucia Range. A prefrontal region of high southerly momentum (>30 m s^{-1}) is apparent in the Doppler velocities at this time (not shown) just offshore wedged between the highest topography in the Santa Lucia Range and the offshore-frontal rainband. Analysis of the radar data suggest that the eastward movement onshore of the line convection and front was impeded by the steep topography.

The simulated radar reflectivity at the 900-mb level for the 16-h time (07/04), shown in Fig. 19a, indicates that the model captured the development of the line convection reasonably well; however, the eastward movement is 2-3 h faster than the observed movement and the orientation of the band is less parallel to the coastal topography than the observations indicate (see Fig. 18a). The band orientation error of ~30° make isolating the topographic influence on the line convection somewhat difficult. The results of Holt et al. (1995) indicate that this phase error is improved through the application of mesoscale data-assimilation techniques for this case. As the simulated front and associated line convection approach the coast, significant deformation of the frontal zone occurs as a result of the steep coastal topography. The simulated 900-mb radar reflectivity for the 17.3-h time (0520 UTC 7 January), shown in Fig. 19b, indicates that the southeastward movement of the line convection is impeded by the topography as evidenced by the southeastward displacement of the rainband well offshore compared to the rainband along the southern end of the Monterey Bay coast and further inland. A well defined prefrontal wedge of strong winds is present immediately seaward of the coastline along the steep topography (Fig. 19b). However, the band orientation error most likely results in a wedge of strong winds wider than observed, as also apparent in the distance offshore of the simulated line convection relative to the observed reflectivity fields for this time (Figs. 18b and 19b). A lower-tropospheric wind-speed maximum, shaded in Fig. 19b, is present along the topography, similar to the radar observations, and is dynamically trapped between the frontal zone to the west and the topography to the east. In the next several hours, the line convection becomes oriented nearly normal to the coast and the southeastward movement is

slowed considerably as the rainband passes the highest topography in the Santa Lucia Range. The simulation of the low-level winds in this case, which were reasonably represented by the model, is not particularly sensitive to the error in the rainband and frontal orientation.

The model simulated radar reflectivity at the 18.7-h time (0640 UTC 7 January), shown in Fig. 19c, indicates that the line convection has intensified somewhat over the high topography as the western edge of the precipitation has advanced eastward. As a result of the rotation of the orientation of the line convection relative to the coastal mountains and topographic blocking of the southeastward movement of the convection, a well defined accumulated precipitation maximum extends upstream from the topography (Fig. 17b). This precipitation spike extends to ~70 km offshore nearly to the boundary of the inner mesh. The offshore precipitation maximum appears to be spurious in this case because the radar observations do not indicate stationary line convection offshore of the highest coastal topography. However, the model results appear to be consistent with other heavy precipitation events observed by NWS forecasters along the central California coast (Dave Reynolds, personal communication). Subsequently upon landfall, the line convection loses its defined structure in both the model simulation and nature.

b. Sensitivity Tests Results

As discussed above, for computational efficiency, the sensitivity tests were performed with a horizontal grid increment of 45-km, 15-km and 5-km on the coarse-, medium- and fine-mesh grids and 30 vertical levels. The control experiment (CTRL) has a configuration identical to the simulation discussed in the previous section except that the horizontal grid increment is larger (Δx=5 km). The second simulation has a terrain elevation of zero and is referred to as NOTOPO. The third experiment is identical to CTRL except the coastline is displaced 100 km westward along a line from Cape Mendicino to Point Conception and is referred to as COAST. In this experiment, the topography is identical to CTRL and is not shifted. The topography is flat in the 100-km zone where the roughness is increased to a typical land value. The goal of this experiment is to attempt to isolate the portion of the

coastal mesoscale response due to low frictional drag over the water and *differential* surface roughness effects along the coast.

The 5-m winds from the three experiments are shown in Figs. 20a-c for the 15-h simulation time (07/03). The low-level wind-speed maximum is in excess of 22 m s^{-1} along southern end of the Monterey Bay in CTRL with a wind direction nearly parallel to the topography and coastline (Fig. 20a) similar to the 2-km grid-increment simulation (Fig. 12d). The wind-speed minimum is positioned across the Monterey Bay similar to the 2-km grid-increment simulation, although the speed in the wake region is somewhat larger than in the observations and in CTRL. The wake is not present in the first (Δx=45 km) or second (Δx=15 km) grid meshes, which should be expected because the width of the wake region is only ~15-20 km.

Without the coastal topography (Fig. 20b), the wind-speed maximum at the 15-h time is reduced by 30%, although maxima remain near the coastline. Also, the results from NOTOPO indicate stronger southwesterly flow along the coast, which underscores the importance of partial blocking of the low-level flow by the coastal mountains. With the absence of the low-level blocking, the strength of the mountain-parallel wind component is reduced considerably. No signature of the flow stagnation region in Monterey Bay is present.

The results from the COAST experiment (Fig. 20c) indicate that the local roughness and surface flux effects along the coastline enhance the topographically forced coastal wind-speed maxima. At the 15-h simulation time (07/03), one wind speed maximum is located near the northern end of the Santa Lucia Range and several new maxima are positioned to the west near the new land-sea interface. The largest region of strong southerly momentum, which is ~26% weaker than CTRL, has shifted 100-km to the west with the new coastline. This maximum appears to be similar to the western-most portion of the LLJ in CTRL. Another wind speed maximum, apparently directly associated with topographical forcing, is positioned just south of the Monterey Peninsula in the lee of the Santa Lucia Range with wind speeds ~22% weaker than CTRL. The wind direction in the region between the new and old coastlines is oriented more down the pressure gradient, consistent with the greater surface momentum flux.

The low-level wind direction for experiment COAST in this region is more parallel to the coastal range than for NOTOPO, which is a signature of the upstream response of the low-level winds to blocking in COAST. Additionally, wind speeds in the region that had surface characteristics representative of water in CTRL are 30-50% weaker along the same region in COAST, which now has surface characteristics of land. The ratio of 5-m wind speeds in the region that was changed from water in CTRL to land in COAST is ~1.3-1.5, which is in agreement with the results of Liu et al. (1984) for a neutral boundary layer. A weakly-defined wind-speed minimum is present in the Monterey Bay, although the structure in COAST has less of an appearance of a wake region than do the CTRL or the 2-km grid-increment simulation. The differences between the COAST and CTRL simulations are greatest immediately near the surface and significantly smaller aloft, in contrast to the differences between NOTOPO and CTRL which are more significant and extend somewhat deeper above the mountain top.

The 24-h accumulated precipitation between 06/12-07/12 for the CTRL, NOTOPO, and COAST simulations are shown in Figs. 21a-c. The accumulated precipitation from the CTRL simulation (Fig. 21a) is similar to the observed rainfall (Fig. 17a) and the 2-km grid-increment simulation (Fig. 17b). The CTRL simulation captures the lee-side precipitation minima near the Monterey Bay area as well as in the Salinas River Valley. The maximum in the Santa Lucia Range of ~73 mm is in closer agreement with the observations than the 2-km grid-increment simulation, which had a maximum accumulated precipitation amount of ~150 mm. The differences between these two simulations in this case underscores the sensitivity of quantitative precipitation forecasting to the grid resolution, which influences numerous factors including the microphysical parameterization and the terrain resolution. The importance of the coastal topography is evident in the NOTOPO simulation (Fig. 21b). A broad area of precipitation greater than 10 mm exists, however there are no maxima exceeding 20 mm along the central California Coast. In addition to moist ascent triggered along the windward slopes of the coastal topography, the sloping isentropes associated with the blocked region provides a

secondary mechanism for precipitation forcing and results in enhancement of the precipitation upstream of the coastal topography in CTRL relative to NOTOPO. The synoptic-scale forcing and the small roughness upstream of the topography accounts for only ~10-20% of the observed precipitation along the Santa Lucia and Santa Cruz Ranges. In the COAST simulation (Fig. 21c), the low-level wind speeds are weaker immediately to the west and upstream of the topography due to the increased boundary-layer momentum flux, which decreases the moist orographic convergence along the coastal ranges. As a result, the precipitation maxima are reduced by nearly 50% in the Santa Cruz Range and by ~12% in the Santa Lucia Range relative to CTRL. The lee-side precipitation minima are nearly as well-defined in COAST as in CTRL.

5. DISCUSSION

Previous observational and modelling studies by Mass and Ferber (1990), Steenburgh and Mass (1996), and Colle and Mass (1996) have documented the existence of asymmetric pressure perturbations around the Olympic Mountains with the flow characterized by small Nh/U. Colle and Mass (1996) attributed the asymmetries in a case of quasi-steady state flow in the vicinity of the Olympic Range to non-linear processes associated with mountain-wave amplification. In the limit of small Nh/U, the character of the flow can be described by linear theory with well defined windward ridging and leeward troughing of identical amplitude (Smith 1980). Smith and Grønås (1993) show that nonlinear effects dominate as the Nh/U increases and stagnation is initiated above the lee slope rather than occurring initially on the windward slope as linear theory predicts. Numerous observational studies have documented cases of lee-side pressure perturbations greater in magnitude than the windward pressure perturbations for flows with moderate values of Nh/U (Reed 1980; Mass and Ferber 1990; Ferber and Mass 1990; Steenburgh and Mass 1996).

The pressure perturbation field due to mesoscale topographic effects for the 15-h time (07/03) (Fig. 22a), computed as the sea level pressure difference between the NOTOPO and CTRL experiments, indicates substantial near-surface positive pressure perturbations exist

upstream and downstream of the coastal mountains. The maximum offshore pressure perturbation exists near the southern end of the Santa Lucia Range with a minimum positioned on the lee-side of the coastal range near the southern end of the Monterey Bay. The strongest offshore pressure perturbation pressure gradient extends from just upstream of the Santa Lucia Range to the southern end of the Monterey Bay. The gradient is coincident with the 5-m wind speed maximum (Fig. 13a). Another region of pressure perturbation gradient is near the eastern portion of the Monterey Bay where a secondary wind-speed maximum exists.

The 5-m wind velocity perturbation due to the mesoscale topography for the 15-h time (07/03) comuputed as the vector wind difference between the NOTOPO and CTRL experiments is shown in Fig. 22b. Topographic blocking results in an increase of over 11 m s^{-1} upstream of the Santa Lucia Range along the coast south of Monterey Bay. This speed maximum is nearly coincident with the large offshore pressure perturbation gradient upstream of the coastal mountains (Fig. 22a) and the simulated 5-m wind speed maximum (Fig. 13a). A secondary maximum is located along the eastern end of the Monterey Bay near the northeastern portion of the Salinas River Valley and is associated with the secondary 5-m wind speed maximum. The flow stagnation region in the vicinity of the Monterey Bay in the lee of the Santa Lucia Range is characterized by relatively small wind velocity perturbations. The width of the wind velocity perturbation maximum is ~120km, which is similar to L_R~140 km at this time in agreement with the results of Pierrehumbert (1984) and Pierrehumbert and Wyman (1985).

The momentum budget in the vicinity of Monterey Bay was computed to further investigate the dynamical balance present near the coastal jet. The momentum equations at 975-mb were diagnosed using model data from the 2-km grid-increment mesh following,

$$\frac{du}{dt} = -g\frac{\partial z}{\partial x} + fv + F_x \qquad (1)$$

$$\frac{dv}{dt} = -g\frac{\partial z}{\partial x} - fu + F_y \qquad (2)$$

where u and v are the horizontal velocity components, z is the geopotential height, g is the acceleration of gravity, and F represents the frictional components. These momentum terms were averaged over a 2-h time period to eliminate high frequency oscillations associated with transitory waves. The frictional components were computed as the average of the residuals.

The vector representation of these momentum terms for the 14-h simulation time (07/02) are shown in Fig. 23 for a portion of the 2-km grid-increment mesh. As parcels approach the Monterey Bay from the south, they are accelerated by a large contribution from the pressure gradient force. This is especially true immediately offshore of Point Sur (location 1 shown in Fig. 23), where the flow is highly ageostrophic and dominated by pressure-gradient accelerations. These strong accelerations extend approximately 20-30 km offshore and are well correlated with the quasi-stationary pressure perturbations induced by the topographic influences. Parcels further offshore to the west of this region (location 2) are dominated by a balance between the pressure gradient, Coriolis force and friction, with relatively small accelerations. As parcels near the coast approach the Monterey Bay, large decelerations occur, with the friction and pressure gradient forces, which greatly contribute to weakening the velocity (location 3) . The reversal in the pressure perturbation gradient (Fig. 23) contributes to parcel deceleration and the eventual formation of the wind-speed minimum that extends across the bay (see Fig. 13a). Along the eastern portion of Monterey Bay and extending into the mouth of the Salinas River Valley, parcels accelerate in response to the perturbation pressure gradient (Fig. 18) near the second wind-speed maximum (location 4). Near the north end of the Monterey Bay on the upwind side of the Santa Cruz Range, smaller parcel acceleration with some areas of deceleration are present again due to the pressure perturbation gradient that reverses in this area (location 5). Offshore of the Santa Cruz Mountains away from the largest pressure perturbations, a balance is maintained between pressure gradient, Coriolis force and friction with relatively small accelerations (location 6).

From the perturbation pressure analysis (Fig. 22) and the analysis of the representative force balances (Fig. 23), the wind-speed minimum over the Monterey Bay appears to be a

manifestation of a complex low-level response to the pressure perturbations induced by the topographically forced flows. The secondary wind-speed maximum along the eastern portion of the Monterey Bay is forced by the low-level airflow interacting with the Gabilan Range and Salinas Valley. Significant channelling through the Salinas Valley is present as well as flow descending down the Gablian Range. The primary wind-speed maximum appears to be enhanced by the steep topography of the Santa Lucia Range.

Although the coastal topography is not high enough to produce complete blocking of the of the low-level flow, the eastward progress of the weakening front and precipitation is impeded and the coastal jet is enhanced due to a topographically blocked response. A schematic of the interaction of the mesoscale frontal features and the topography is shown in Fig. 24a. As the front approaches the coastal topography at a significant angle, the onshore movement of the southern portion of the front is slowed by low-level blocking effects. The shallow depth of the front, large static stability ahead of the front, and the steep coastal topography contribute to the topographic modulation of the onshore movement of the front in agreement with the results of Davies (1984) and Schumann (1987). The southerly prefrontal jet is then enhanced by the topographically modulated mountain-normal pressure gradient (Fig. 24b). The coastal jet (J) is centered near the base of a sloping stable layer, which is a manifestation of the low-level blocking. As winds veer with height, the flow above the stable region ascends the coastal mountains and adds complex pressure perturbation anomalies to the mass field and ultimately to the low-level winds.

5. SUMMARY AND CONCLUSIONS

In this study, the Navy's next-generation operational mesoscale model, COAMPS, is used to study the influence of the complex topographical forcing of the coastal mountains of central California on an intense coastal jet and narrow cold-frontal rainband. The synoptic-scale forcing associated with this weather system acted in concert with the mesoscale forcing associated with coastal processes to produce damaging coastal winds and heavy precipitation in the coastal mountains.

A triply-nested simulation with a minimum horizontal grid increment of 2 km captured the formation, evolution and structure of the coastal jet system. In a time period of less than 6 h, the wind speeds increase by 10-15 m s^{-1} along the coast. The near-surface coastal winds are in general parallel to the topography, as a manifestation of low-level blocking, with a maximum of ~22 m s^{-1} near the northern-most extent of the steep coastal topography south of Monterey. The coastal jet is comprised of a well-defined maximum in the mountain-parallel component at 975 mb near the base of a sloping stable layer, which is a manifestation of the low-level blocking. Above the blocked layer, the wind direction veers with height and the onshore cross-mountain component increases. The combination of low-level blocked flow and cross-mountain flow near ridge top induces significant perturbation pressure anomalies. Force balance analysis suggests that the coastal jet is a complex response to the large along-shore perturbation pressure gradients manifested by the topographically forced flow. Additionally, flow splitting and a well-defined wake in the lee of the coastal range, which is simulated by the model and consistent with observations, is important in defining the northern extent and horizontal scale of the coastal jet by modulation of the pressure perturbations. Model results suggest that the wake may be a response to the topographically-induced perturbation pressures.

The nonhydrostatic model simulation captures the development and movement of line convection associated with the front. The simulated accumulated precipitation is in general too large in the coastal mountains when compared with a mesoscale network of rainguage observations along the coastal mountains, although the mesoscale precipitation structure is simulated reasonably well. However, the difference between the observed and simulated orientation of the frontal rainband is ~30°. This implies that the accurate prediction of the low-level winds in this case, which were reasonably represented by the model, is not particularly sensitive to the error in the rainband and frontal orientation. The observed and simulated radar reflectivity indicate that the movement of the line convection is impeded by the steep coastal topography. The low-level blocking results in the formation of a wedge-shaped region

of strong along-shore flow parallel to the coastal topography. The low-level blocking results in a coastal jet that is dynamically trapped between the steep coastal mountains and the front.

Sensitivity results underscore the importance of the coastal topography in the enhancement of the coastal jet and precipitation. Topography accounts for a ~45% increase in the near-surface wind speeds. Sensitivity tests suggest that the contrasting frictional drag over the water and land is important in the generation of the large near-surface wind maximum. The small roughness over the water upstream of the coastal topography acts to modulate the low-level winds to a direction more conducive for blocking.

The results of this study indicate a promising future for the simulation of fine-scale structures associated with topographically forced flows in the coastal zone. As demonstrated in this study, sophisticated nonhydrostatic models such as COAMPS, are capable of successfully simulating and predicting these complex flows in an operational environment. Additional evaluations of these mesoscale models are needed to fully assess the mesoscale predictability in the coastal zone. Future studies will greatly benefit from special field program validation data collected in complex coastal environments such as the COAST (Coastal Observation and Simulation with Topography) experiment, which took place in December of 1993 and 1995 along the coastal mountains of the Pacific Northwest.

6. ACKNOWLEDGMENTS

This research was supported by the Naval Research Laboratory's program element 0602704N and the Coastal Meteorology ARI program element 0601153N. Comments and suggestions from Clifford Mass, Fred Sanders and an anonymous reviewer greatly improved the manuscript. Numerous discussions with M.A. Shapiro of NOAA/ETL were invaluable in developing the schematic conceptualization for this case. Beneficial discussions with Robin Brody, Steve Burk, Simon Chang, and Richard Hodur of NRL contributed to improvements in the manuscript. Special data used in this study were graciously provided by Richard Lind and Wendell Nuss of the Naval Postgraduate School, Byron Mauler of the Pacific Gas and Electric Corp., Dave Reynolds of the NWS-Monterey, Leslie Rosenthal of the Monterey Bay Research

Institute, and John Stromel of the Water Resources Agency of Monterey County. Steve Bishop and Robin Brody assisted with the preparation of the figures. This work was supported in part by a grant of HPC time from the DoD Shared Resource Center, U.S. Army Corps of Engineers Waterways Experiment Station HPC Center and performed on a Cray C-90.

REFERENCES

Baker, N.L., 1992: Quality control for the Navy Operational Atmospheric Database. *Wea. Forecasting*, **7**, 250-261.

Banta, R.M., L.D. Olivier, and D.H. Levinson, 1993: Evolution of the Monterey Bay sea-breeze layer as observed by pulsed Doppler lidar. *J. Atmos. Sci.*, **50**, 3959-3982.

Barker, E.H., 1992: Design of the Navy's multivariate optimum interpolation analysis system. *Wea. Forecasting*, **7**, 220-231.

Bell, G.D., and L.F. Bosart, 1988: Appalacian cold air daming. *Mon. Wea. Rev.*, **116**, 137-161.

Bjerknes, J., and H. Solberg, 1921: Meteorological conditions for the formation of rain. *Geofys. Publik.*, **2(3)**, 1-60.

Bond, N.A. and M.A. Shapiro, 1991: Research aircraft observations of the mesoscale and microscale structure of a cold front over the eastern Pacific Ocean. *Mon. Wea. Rev.*, **119**, 3080-3094.

Burk, S.D., and W.T. Thompson, 1996: The summertime low-level jet and marine boundary layer structure along the California coast. *Mon. Wea. Rev.*, **124**, 668-686.

Colle, B.A., and C.F. Mass, 1996: An observational and modeling study of the interaction of low-level southwesterly flow with the Olympic Mountains during COAST IOP 4. *Mon. Wea. Rev.*, **124**, 2152-2175.

Davies, H.C., 1984: On the orographic retardation of a cold front. *Beitr. Phys. Atmosph.*, **57**, 409-418.

Doyle, J.D. and T.T. Warner, 1993: A three-dimensional numerical investigation of a Carolina coastal low-level jet during GALE IOP 2. *Mon. Wea. Rev.*, **121**, 1030-1047.

Ferber, G.K., and C.F. Mass, 1990: Surface pressure perturbations produced by an isolated mesoscale topographic barrier. Part II. Influence on regional circulations. *Mon. Wea. Rev.*, **118**, 2597-2606.

Gal-Chen, T., and R.C.J. Somerville, 1975: On the use of a coordinate transformation for the solution of the Navier-Stokes equations. *J. Comput. Phys.*, **17**, 276-309.

Harshvardhan, R. Davies, D. Randall, and T. Corsetti, 1987: A fast radiation parameterization for atmospheric circulation models. *J. Geophys. Res.*, **92**, 1009-1015.

Hobbs, P.V., and P.O.G. Persson, 1982: The mesoscale and microscale structure and organization of clouds and precipitation in midlatitude cyclones. Part V: The substructure of narrow cold-frontal rainbands. *J. Atmos. Sci.*, **39**, 280-295.

Hodur, R.M., 1993: Development and testing of the Coupled Ocean/Atmosphere Mesoscale Prediction System (COAMPS). NRL/MR/7533-93-7213, Naval Research Laboratory, 84 pp. [Available from Naval Research Laboratory, Monterey, CA 93943-5502]

Hogan, T.F., T.E. Rosmond, R. Gelaro, 1991: The NOGAPS forecast model: A technical description. NOARL Report 13, Naval Oceanographic and Atmospheric Research Laboratory, 220 pp. [Available from Naval Research Laboratory, Monterey, CA 93943-5502]

Holt, T.H.,1996: Mesoscale forcing of a boundary layer jet along the California coast. *J. Geophys. Res.*, **101**, 4235-4254.

Holt, T.H., J.D. Doyle, and R.M. Hodur, 1995: Sensitivity of numerical simulations in complex terrain to data assimilation. *Preprints of the Seventh Conf. on Mountain Meteorology*, 17-21 July 1995, Breckenridge, CO., 239-244.

Hoinka, K.P., and R.K. Smith, 1988: A dry cold-front over southern Bavaria. *Weather*, **43**, 255-261.

Hoinka, K.P., and H. Volkert, 1992: Fronts and the Alps: Findings from the Front Experiment 1987. *Meteorol. Atmos. Phys.*, **48**, 51-75.

Kain, J.S., and J.M. Fritsch, 1990: A one-dimensional entraining/detraining plume model and

its application in convective parameterization. *J. Atmos. Sci.*, **47**, 2784-2802.

Kurz, M., 1990: The influence of the Alps on the structure and behavior of cold fronts over southern Germany. *Meteorol. Atmos. Phys.*, **43**, 61-68.

Longley, R.W., 1975: Precipitation in valleys. *Weather*, **30**, 294-300.

Liu, P.C., D.J. Schwab and J.R. Bannett, 1984: Comparison of a two-dimensional wave prediction model with synoptic meansurements in Lake Michigan. *J. Phys. Oceanogr.*, **14**, 1514-1518.

Mass, C.F, and G.K. Ferber, 1990: Surface pressure perturbations produced by an isolated mesoscale topographic barrier. Part I: General characteristics and dynamics. *Mon Wea. Rev.*, **118**, 2579-2596.

Neiberger, M., 1960: The relation of air-mass structure to the field of motion over the eastern North Pacific Ocean in summer. *Tellus*, **12**, 31-40.

Nordø, J., and Hjortnæs, K., 1966: Statistical studies of precipitation on local, national, and continental scales. *Geofys. Publ.*; **16**, (12).

Pierrehumbert, R.T., and B. Wyman, 1985: Upstream effects of mesoscale mountains. *J. Atmos. Sci.*, **42**, 977-1003.

Overland, J.E., 1984: Scale analysis of marine winds in straits and along mountainous coasts. *Mon Wea. Rev.*, **112**, 2532-2536.

Overland, J.E., and N. Bond, 1993: The influence of coastal orography: The Yakutat storm. *Mon Wea. Rev.*, **121**, 1388-1397.

Overland, J.E., and N. Bond, 1995: Observations and scale analysis of coastal wind jets. *Mon. Wea. Rev.*, **123**, 2934-2941.

Reed, R.J., 1980: Destructive winds caused by an orographically induced mesoscale cyclone. *Bull. Amer. Meteor. Soc.*, **61**, 1346-1355.

Rogers, D.P., 1995: Coastal meteorology, *Rev. of Geophys.: U.S. National Report to International Union of Geodesy and Geophysics*, **33**, 880-895.?

Rotunno, R., J.A. Curry, C.W. Fairall, C.A. Friehe, W.A. Lyons, J.E. Overland, R.A. Pielke,

D.P. Rogers, S.A. Stage, 1992: *Coastal Meteorology, A review of the state of the science*, National Academy Press, Washington D.C., 99 pp.

Rutledge, S.A., and P.V. Hobbs, 1983: The mesoscale and microscale structure of organization of clouds and precipitation in midlatitude cyclones. VIII: A model for the "seeder-feeder" process in warm-frontal rainbands. *J. Atmos. Sci.*, **40**, 1185-1206.

Schumann, U., 1987: Influence of mesoscale orography on idealized cold fronts. *J. Atmos. Sci.*, **44**, 3423-3441.

Smith, R.B., 1979: The influence of mountains on the atmosphere. *Adv. Geophys.*, **21**, 87-230.

Smith, R.B., 1980: Linear theory of hydrostatic flow over an isolated mountain. *Tellus*, **32**, 348-364.

Smith, R.B., 1989: Hydrostatic airflow over mountains, *Advances in Geophysics*, **31**, 1-41.

Smith, R.B., and S. Grønås, 1993: Stagnation points and bifurcation in 3-D mountain airflow. *Tellus*, **45A**, 28-43.

Smith, R.B., and D.F. Smith, 1995: Pseudoinviscid wake formation by mountains in shallow-water flow with a drifting vortex. *J. Atmos. Sci.*, **52**, 436-454.

Smolarkiewicz, P.K., R.M. Rasmussen, and T.L. Clark, 1988: On the dynamics of Hawaiian cloud bands: Island forcing. *J. Atmos. Sci.*, **45**, 1872-1905.

Smolarkiewicz, P.K., and R. Rotunno, 1989: Low Froude number flow past three-dimensional obstacles. Part I: Baroclinically generated lee vortices. *J. Atmos. Sci.*, **46**, 1154-1164.

Smolarkiewicz, P.K., and R. Rotunno, 1990: Low Froude number flow past three-dimensional obstacles. Part I: Upwind flow reversal zone. *J. Atmos. Sci.*, **47**, 1498- 1511.

Steenburgh, W.J., and C.F. Mass, 1996: Interaction of an intense extratropical cyclone with coastal orography. *Mon. Wea. Rev.*, **124**, 1329-1352.

Therry, G., and P. Lacarrére, 1983: Improving the eddy kinetic energy model for planetary boundary layer description. *Bound.-Layer Meteor.*, **25**, 63-88.

Trüb, J., and H.C. Davies, 1995: Flow over a mesoscale ridge: pathways to regime transition.

Tellus, **47A**, 502-524.

Volkert, H.L., L. Weickmann, and A. Tafferner, 1991: The "Papal Front" of 3 May 1987 - A remarkable example of frontogenesis near the Alps. *Quart. J. Roy. Meteor. Soc.*, **117**, 125-150.

Williams, R.T., M.S. Peng, and D.A. Zankofsi, 1992: Effects of topography on fronts. *J. Atmos. Sci.*, **49**, 287-305.

Zhender, J.A., and P.R. Bannon, 1988: Frontogenesis over a mountain ridge. *J. Atmos. Sci.*, **45**, 628-644.

FIGURE CAPTIONS

Fig. 1. Terrain and geographical features of the central California coast (From Banta et al., 1993). Terrain isopleths are plotted every 250 m. Elevations between 500 and 1000 m are lightly shaded and elevations above 1000 m are depicted by the dark shading.

Fig. 2. Numerical model grid-mesh domain and topography for the (a) second grid mesh (Δx=6 km) and (b) third grid mesh (Δx=2 km). The terrain isopleth interval is 250 m. The tick mark interval around the border is every 5 grid points. The lines A-A', B-B', and C-C' show the orientation of vertical cross sections on which the model simulation is displayed.

Fig. 3. Sea-level pressure and frontal analysis for (a) 1200 UTC 6 January 1995 (06/12) and (b) 07/00. The isobars are plotted every 4 mb. The tick mark interval around the border is 45 km.

Fig. 4. 850-mb potential temperature analysis for (a) 06/12 and (b) 07/00. The isentropes are plotted every 1 K.

Fig. 5. 500-mb geopotential height and 300-mb wind speed analyses for (a) 1200 UTC 6 January 1995 (06/12) and (b) 07/00. The geopotential height contours are plotted in solid contours every 60 m. The 300-mb isotachs are dashed contours with an interval of 10 m s^{-1}.

Fig. 6. Infrared satellite image for 07/00.

Fig. 7. Model-simulated 900-mb equivalent potential temperature (K) for the second grid-mesh domain (Δx=6 km) for (a) 6 h (06/18), (b) 12 h (07/00), and (c) 18 h (07/06). The contour interval is 1 K. The tick mark interval is 30 km or 5 grid points.

Fig. 8. Model-simulated 900-mb wind speed and direction for the second grid-mesh domain (Δx=6 km) for (a) 6 h (06/18), (b) 12 h (07/00), and (c) 18 h (07/06). The isotach interval is 2.5 m s^{-1}. Wind speeds greater than 25 m s^{-1} are shaded.

Fig. 9. Vertical cross section of model-simulated potential temperature (K) for (a) 6 h

(06/18) along axis A-A' (Fig. 2a), (b) 12 h (07/00) along axis A-A', and (c) 18 h (07/06) along axis B-B'. The isentrope interval is 1 K. Tick marks are plotted along the abscissa every 50 km.

Fig. 10. Model-simulated wind speed parallel to the vertical cross section plane (mountain-normal component) for (a) 6 h (06/18) along axis A-A' (Fig. 2a), (b) 12 h (07/00) along axis A-A', and (c) 18 h (07/06) along axis B-B'. The isotach interval is 2 m s^{-1}. Tick marks are plotted along the abscissa every 50 km.

Fig. 11. Model-simulated wind speed normal to the vertical cross section plane (mountain-parallel component) for (a) 6 h (06/18) along axis A-A' (Fig. 2a), (b) 12 h (07/00) along axis A-A', and (c) 18 h (07/06) along axis B-B'. The isotach interval is 2 m s^{-1}. Tick marks are plotted along the abscissa every 50 km.

Fig. 12. Model-simulated 5-m wind speed and direction for the inner grid-mesh domain (Δx=2 km) for (a) 6 h (06/18), (b) 9 h (06/21), (c) 12 h (07/00), and (d) 15 h (07/03). The isotach interval is 2.5 m s^{-1}. Wind speeds greater than 15 m s^{-1} are shaded. Model-simulated wind speed and direction are shown by the vectors plotted every 10 grid points. Surface wind observations of interest are represented by the wind barbs, with one full barb equivalent to 5 m s^{-1}. The tick mark interval is 10 km or 5 grid points.

Fig. 13. Subsection of the model inner grid-mesh domain (Δx=2 km) of the 13-h simulated (a) 5-m wind speed and (b) 5-m streamlines. The isotach interval in (a) is 1 m s^{-1}. Model terrain height is plotted every 100 m in (b). Surface wind observations are represented by the wind barbs, with one full barb equivalent to 5 m s^{-1}. Station observation identifications are plotted in (a). Tick marks are plotted around the border every grid point or 2 km.

Fig. 14. Time series between 06/18 and 07/06 of observed surface wind speed for buoy M1 (dashed), buoy M2 (thin solid), and Moss Landing (ML, heavy solid).

Fig. 15. Vertical cross section along axis C-C' (see Fig. 2b) of model-simulated potential

temperature (K) for the 13-h simulation time (07/01). The isentrope interval is 1 K. Turbulent kinetic energy greater than 0.5 $m^2 s^{-2}$ is shaded. Tick marks are plotted along the abscissa every 10 km.

Fig. 16. Wind speed and direction displayed as (a) time-height section of hourly observations between 06/12 and 07/11 from the Naval Postgraduate School's 915 MHz wind profiler located at Fort Ord (location FO in Fig. 6a) and (b) time-pressure section between 0 h (06/12) and 24 h (07/12) of model-simulated winds interpolated to the Fort Ord site. Geopotential heights for a standard atmosphere are shown in (b). One full barb is equivalent to 5 m s^{-1} and a flag represents 25 m s^{-1}. Frontal passage is indicated by the caret in (b).

Fig. 17. The 24-h accumulated (a) observed precipitation analysis and (b) model-simulated precipitation between 06/12 and 07/12. The isohyet interval is 25 mm. The 10 and 20 mm isohyets are shown as dashed isopleths. Station observations are plotted in mm in (a). Precipitation in excess of 75 mm is shaded in (b). Only a portion of the inner-computational mesh is shown in (b).

Fig. 18. Radar reflectivity (dBZ) from the National Weather Service WSR-88D Doppler radar data for (a) 0600 UTC 7 January and (b) 0653 UTC 7 January. The isopleth interval is 10 dBZ beginning with 20 dBZ.

Fig. 19. Model-simulated 900-mb radar reflectivity (dBZ) for the (a) 16-h time (0400 UTC 7 January), (b) 17.3 h time (0520 UTC 7 January), and (c) 18.7 h time (0640 UTC 7 January). The isopleth interval is 10 dBZ. The 975-mb wind speed in excess of 30 m s^{-1} is shaded in (b).

Fig. 20. Model-simulated 5-m wind speed and direction for the inner grid-mesh domain (Δx=5 km) for the 15-h simulation time (07/03) for (a) CTRL, (b) NOTOPO, and (c) COAST. The isotach interval is 2.5 m s^{-1}. Wind speeds greater than 15 m s^{-1} are shaded. Model-simulated wind speed and direction are shown by the vectors plotted every 7 grid points. The tick mark interval is 10 km or 2 grid points.

Fig. 21. Model-simulated 24-h accumulated precipitation valid at 07/12 for the inner grid-mesh domain (Δx=5 km) for (a) CTRL, (b) NOTOPO, and (c) COAST. The contour interval is 10 mm.

Fig. 22. The 15 h (07/03) (a) sea-level pressure perturbation (difference field CTRL minus NOTOPO) and (b) 5-m wind velocity perturbation (difference field CTRL minus NOTOPO) for a portion of the inner mesh (Δx=2 km). The isobar interval in (a) is 0.5 mb and the isotach interval in (b) is 1 m s^{-1}.

Fig. 23. Vector representation of momentum-budget terms at 975 mb valid at the 14-h simulation time (07/02) for a portion of the inner mesh (Δx=2 km). The velocity, pressure gradient force, Coriolis force, and parcel acceleration are labeled **V**, **P**, **C**, and **A**, respectively. The friction or residual vector is labeled by **F**.

Fig. 24. Schematic diagram showing the evolution of a surface frontal system as it impinges upon coastal topography (a). The land surface is shown by the hatched region. The coastally trapped jet is shaded. A schematic vertical cross section of potential temperature through the front and coastal jet (along axis AB). The coastal jet is shaded with schematic wind barbs as shown.

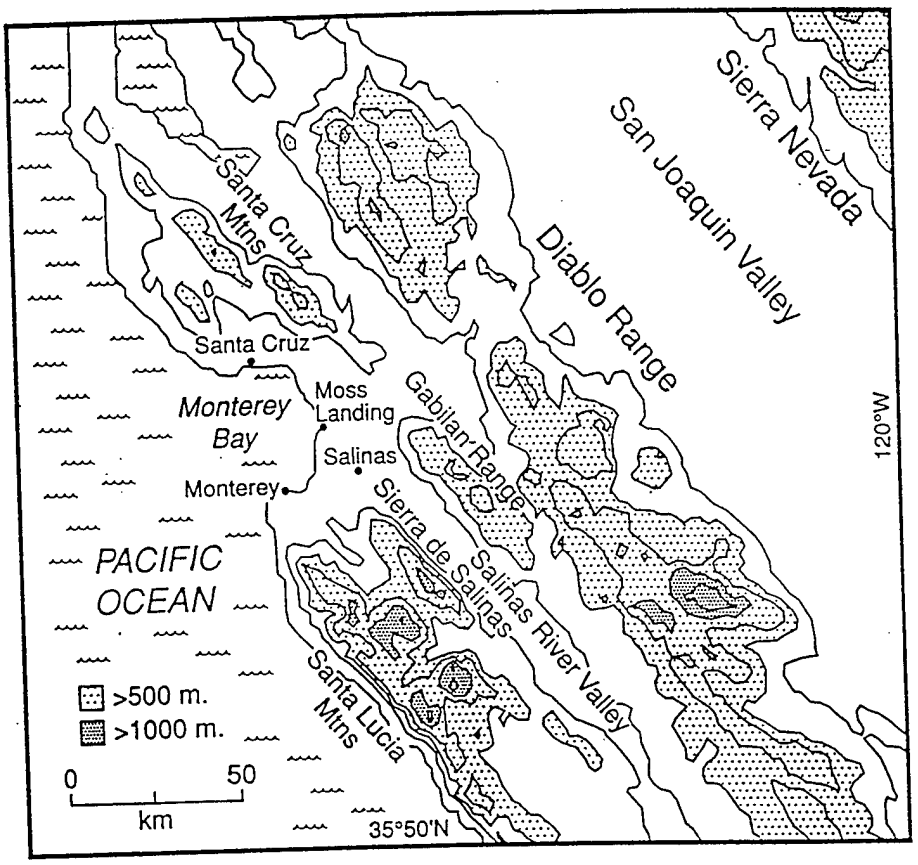

Fig. 1. Terrain and geographical features of the central California coast (From Banta et al., 1993). Terrain isopleths are plotted every 250 m. Elevations between 500 m and 1000 m are lightly shaded and elevations above 1000 m are depicted by the dark shading.

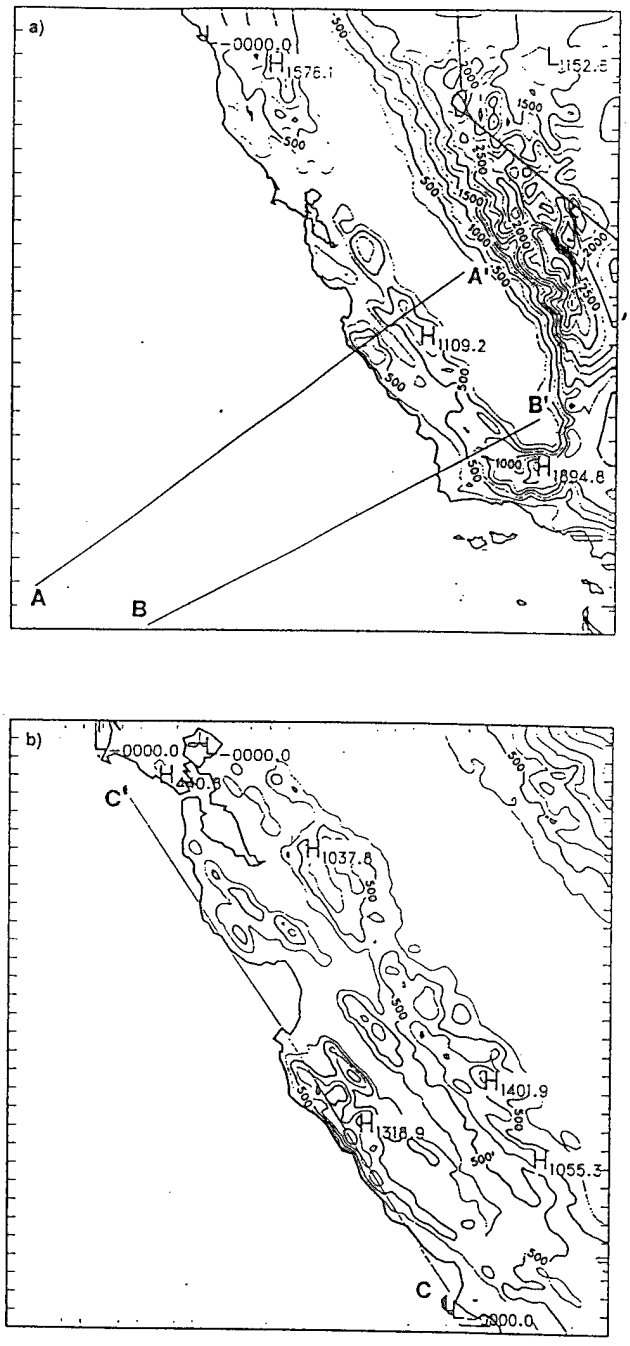

Fig. 2. Numerical model grid-mesh domain and topography for the (a) second grid mesh (Δx=6 km) and (b) third grid mesh (Δx=2 km). The terrain isopleth interval is 250 m. The tick mark interval around the border is every 5 grid points. The lines A-A', B-B', and C-C' show the orientation of vertical cross sections on which the model simulation is displayed.

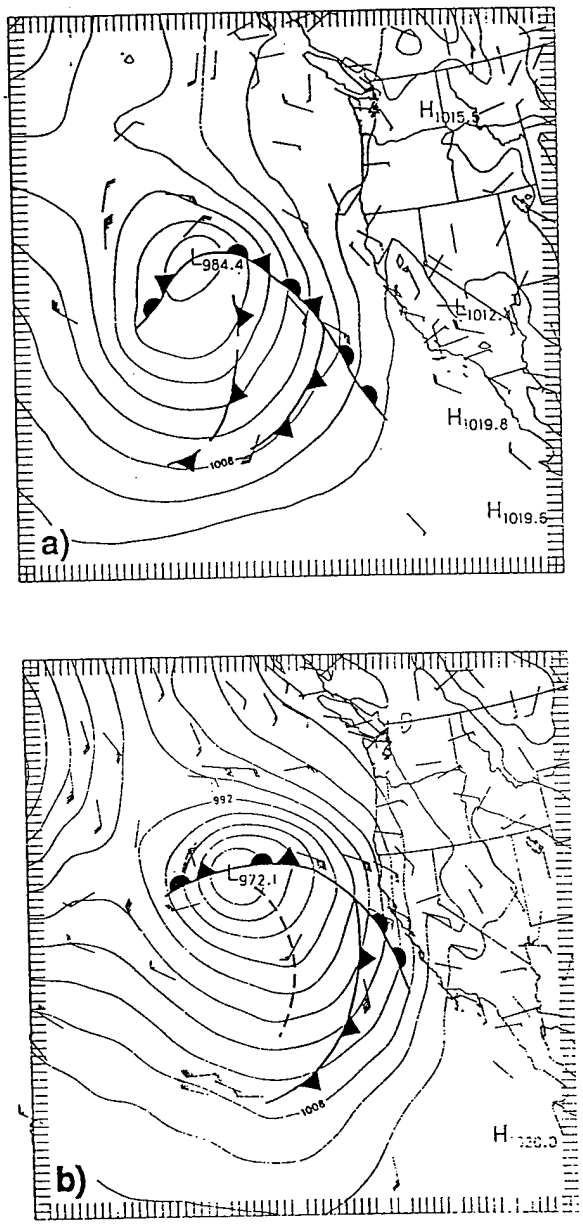

Fig. 3. Sea-level pressure and frontal analyses for (a) 1200 UTC 6 January 1995 (06/12) and (b) 07/00. The isobars are plotted every 4 mb. The tick mark interval around the border is 45 km.

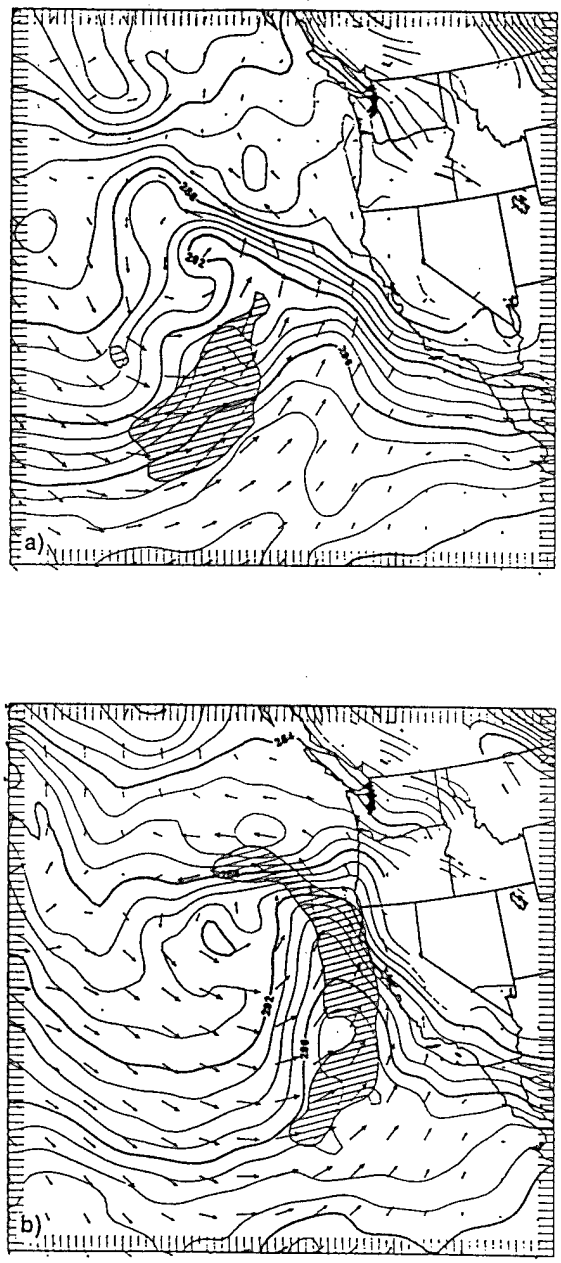

Fig. 4. 850-mb potential temperature analysis for (a) 06/12 and (b) 07/00. The isentropes are plotted every 1 K.

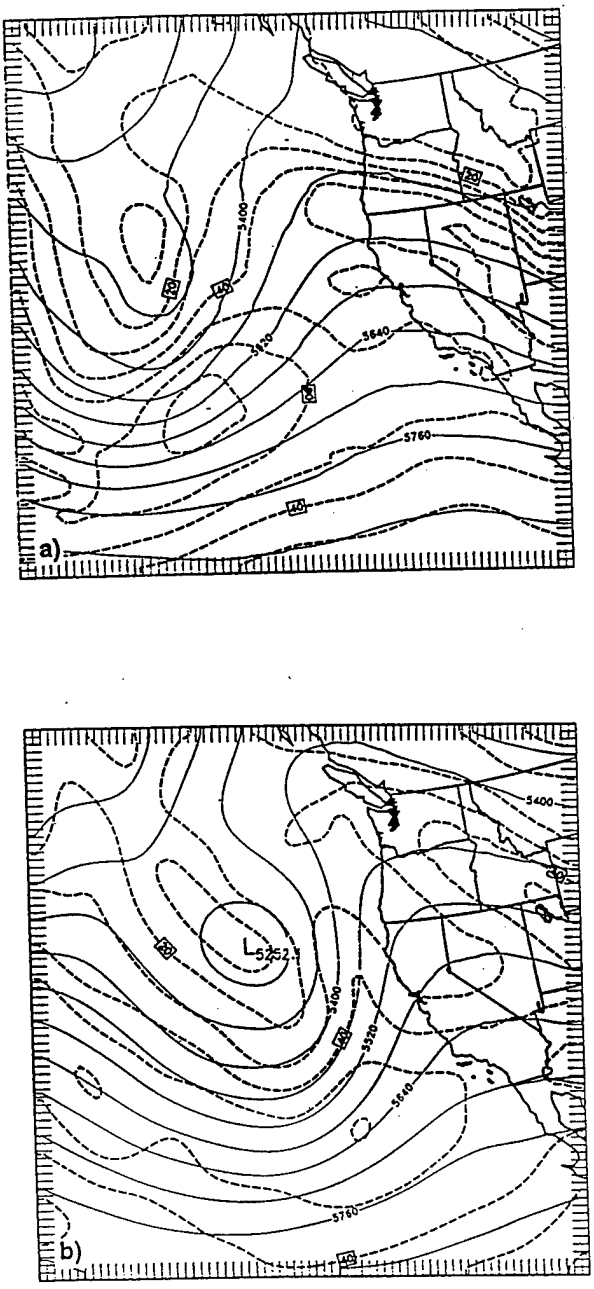

Fig. 5. 500-mb geopotential height and 300-mb wind speed analysis for (a) 1200 UTC 6 January 1995 (06/12) and (b) 07/00. The geopotential height contours are plotted in solid contours every 60 m. The 300-mb isotachs are dashed contours with an interval of 10 m s^{-1}.

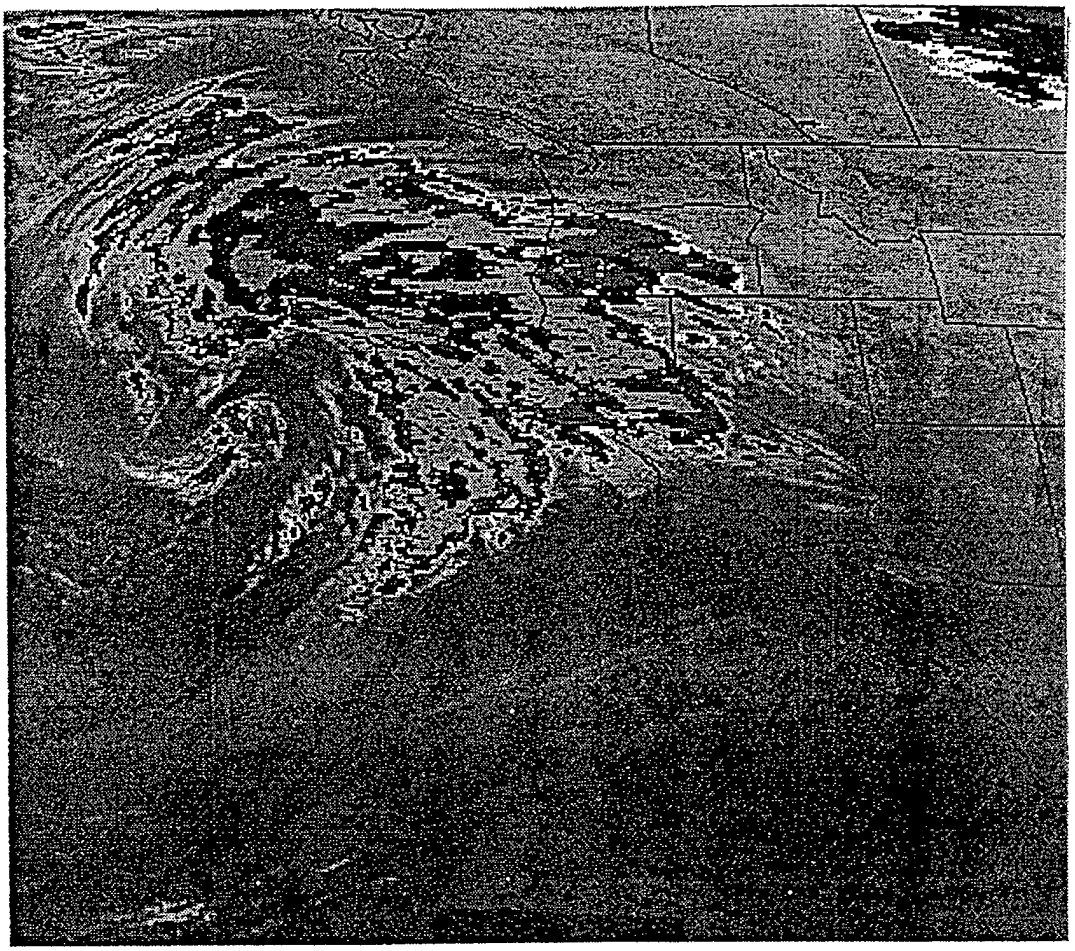

Fig. 6. Infrared satellite image for 07/00.

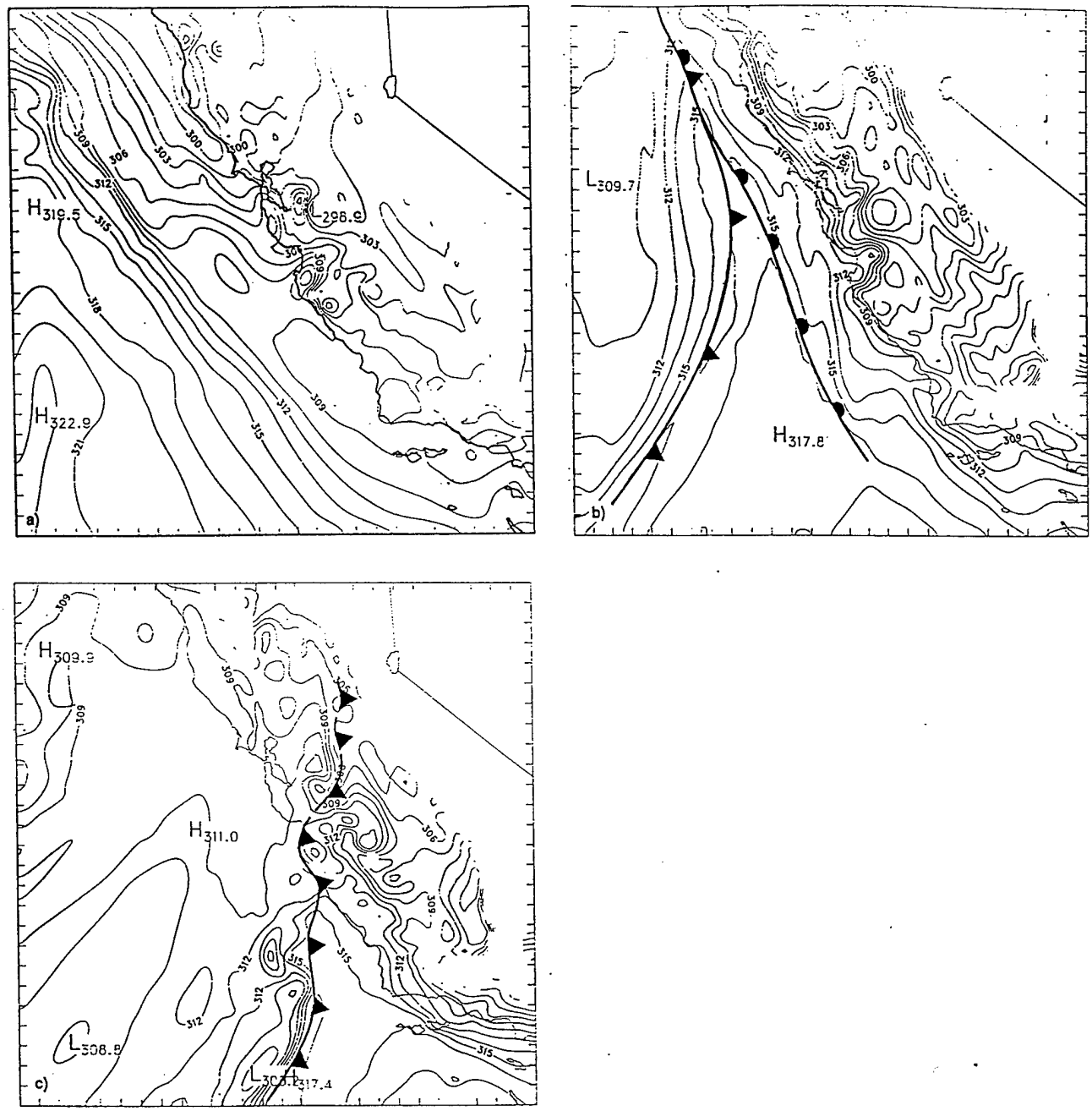

Fig. 7. Model-simulated 900-mb equivalent potential temperature (K) for the second grid-mesh domain (Δx=6 km) for (a) 6 h (06/18), (b) 12 h (07/00), and (c) 18 h (07/06). The contour interval is 1 K. The tick mark interval is 30 km or 5 grid points.

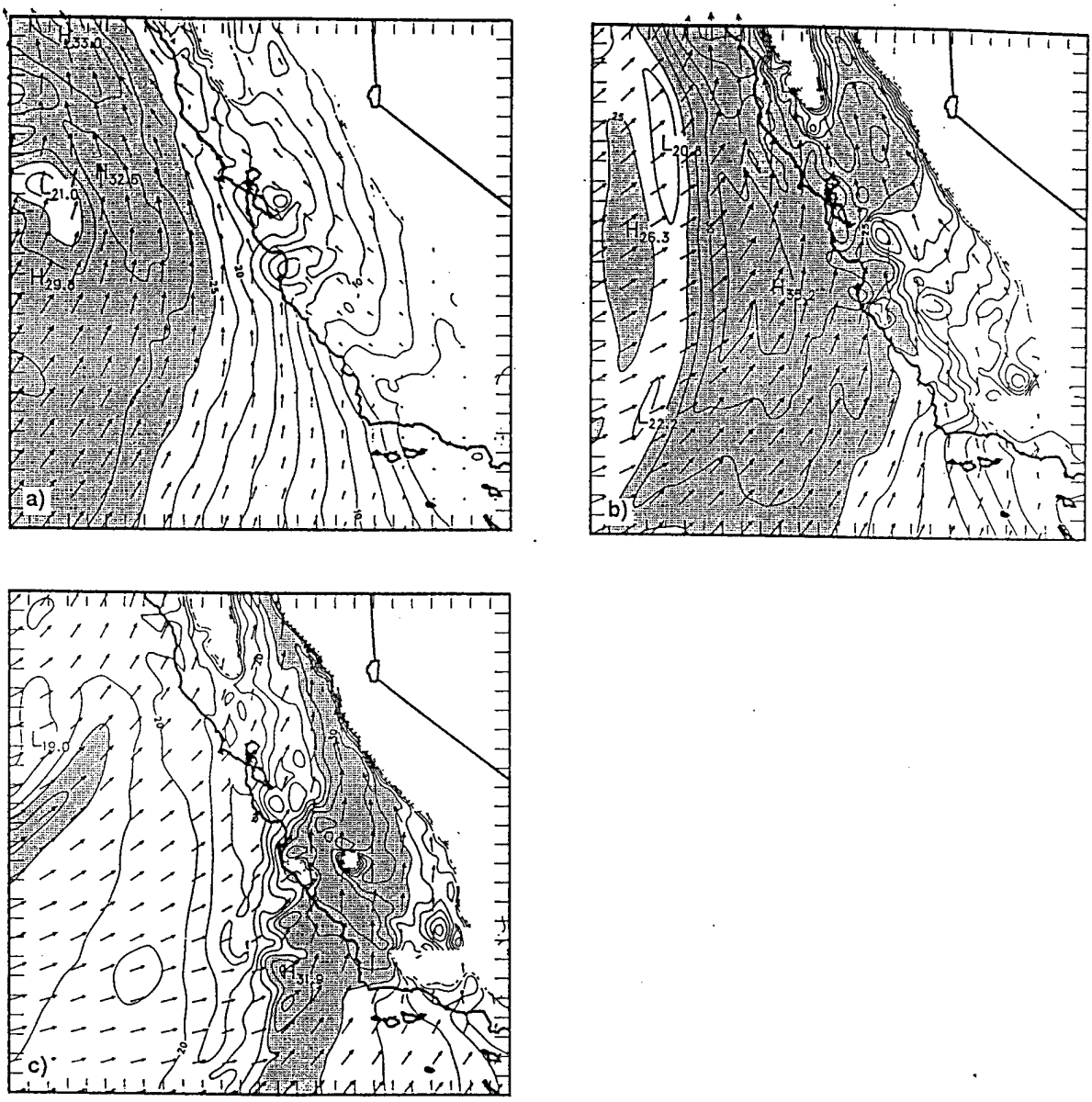

Fig. 8. Model-simulated 900-mb wind speed and direction for the second grid-mesh domain (Δx=6 km) for (a) 6 h (06/18), (b) 12 h (07/00), and (c) 18 h (07/06). The isotach interval is 2.5 m s^{-1}. Wind speeds greater than 25 m s^{-1} are shaded.

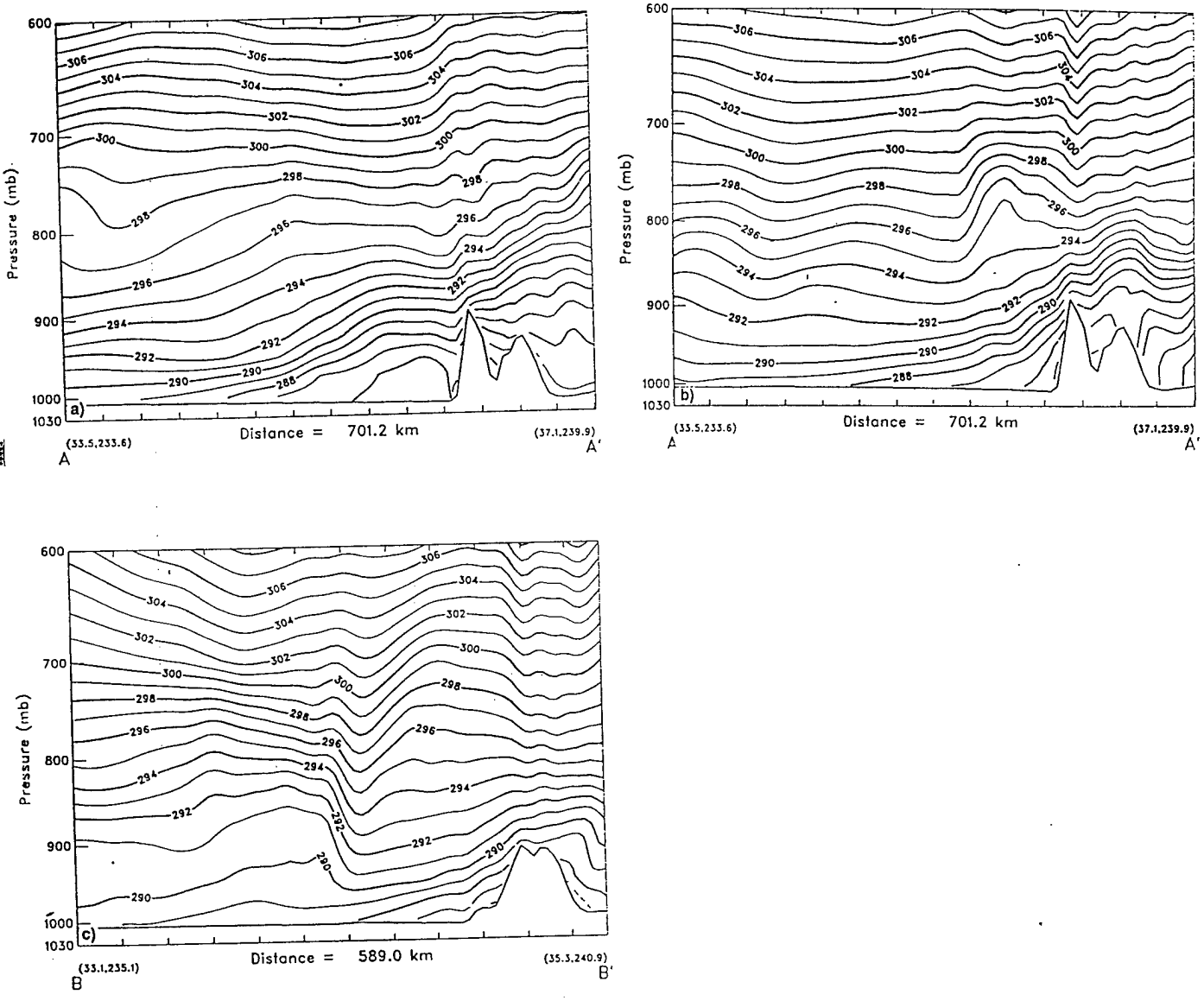

Fig. 9. Vertical cross section of model-simulated potential temperature (K) for (a) 6 h (06/18) along axis A-A' (Fig. 2a), (b) 12 h (07/00) along axis A-A', and (c) 18 h (07/06) along axis B-B'. The isentrope interval is 1 K. Tick marks are plotted along the abscissa every 50 km.

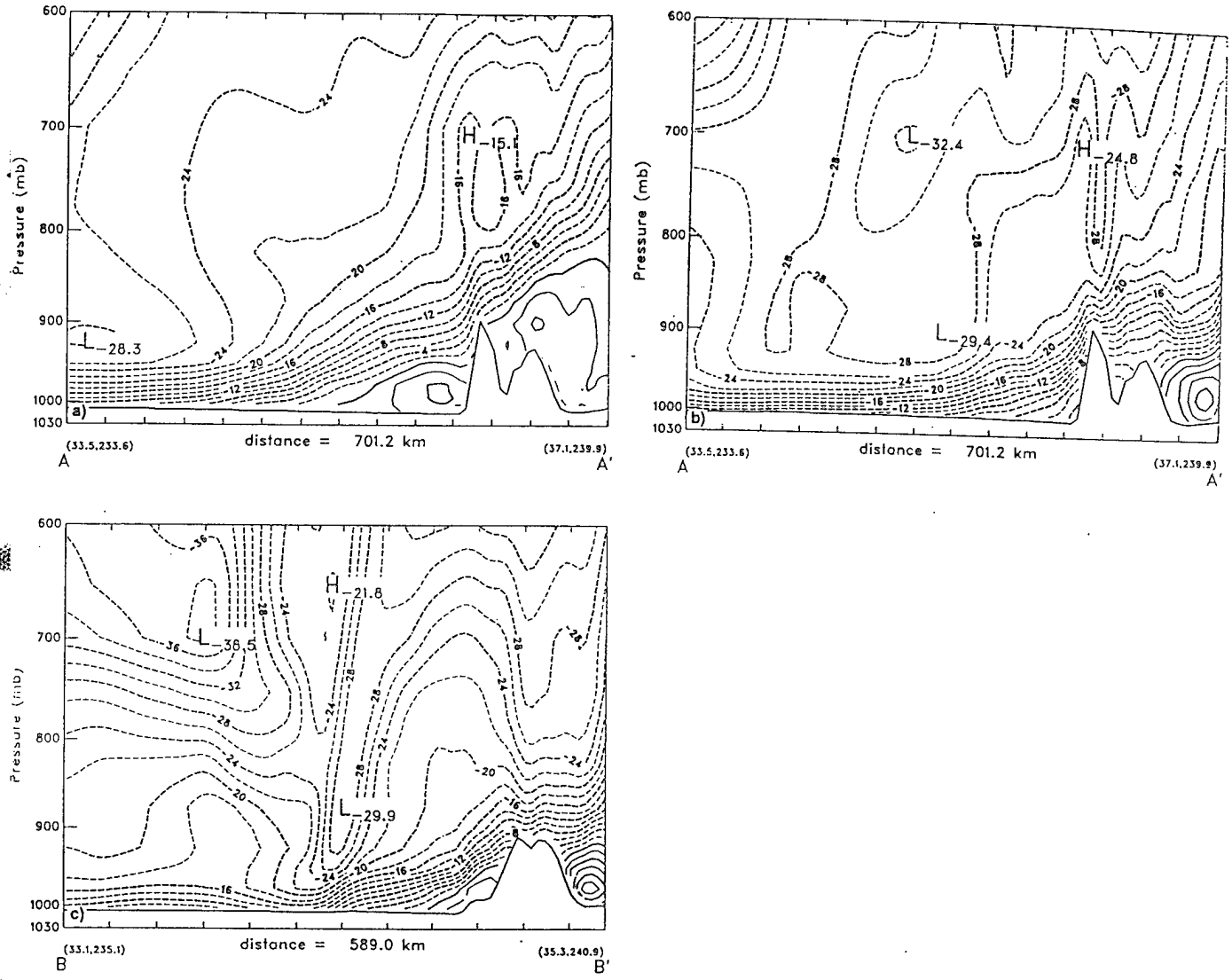

Fig. 10. Model-simulated wind speed parallel to the vertical cross section plane (mountain-normal component) for (a) 6 h (06/18) along axis A-A' (Fig. 2a), (b) 12 h (07/00) along axis A-A', and (c) 18 h (07/06) along axis B-B'. The isotach interval is 2 m s^{-1}. Tick marks are plotted along the abscissa every 50 km.

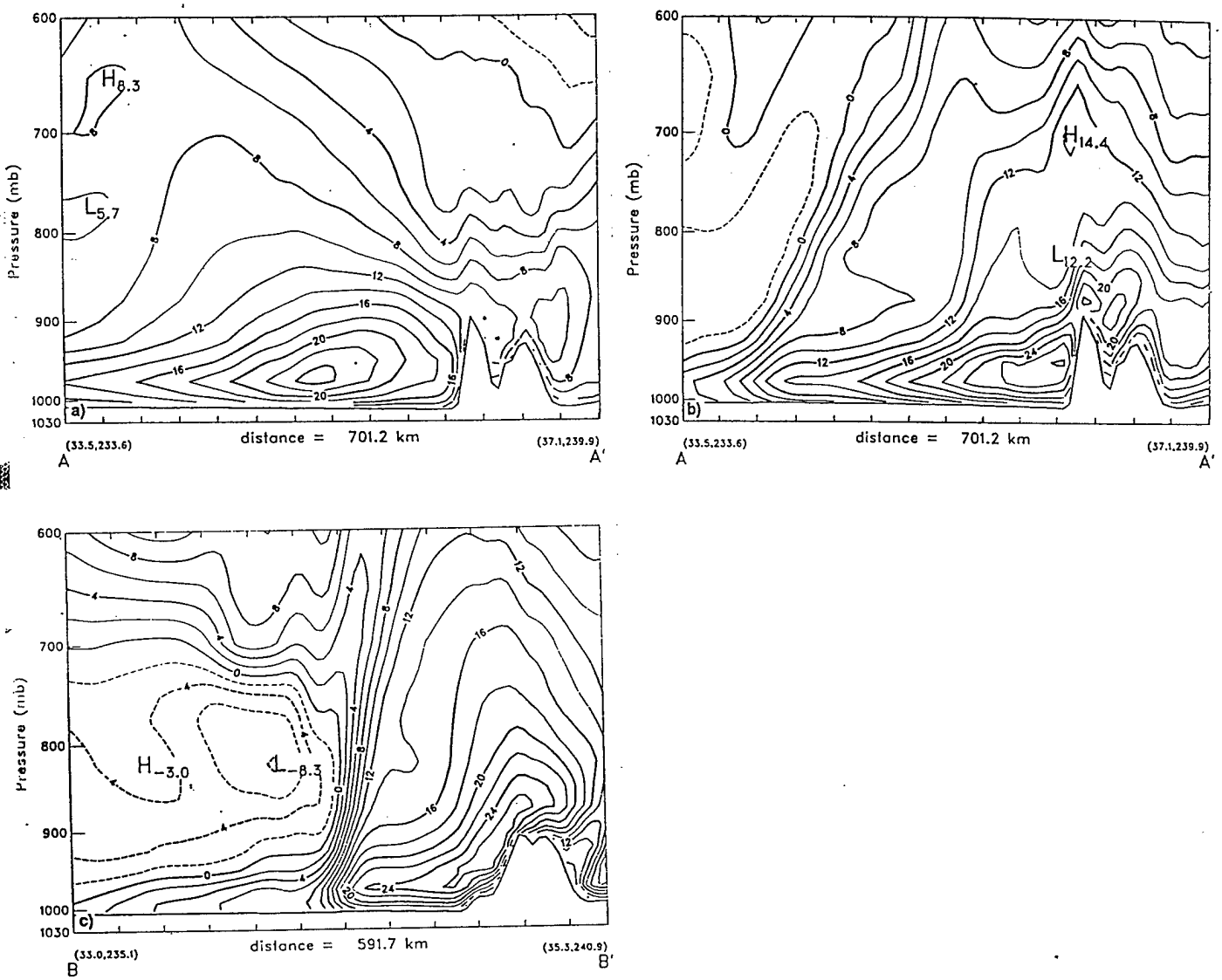

Fig. 11. Model-simulated wind speed normal to the vertical cross section plane (mountain-parallel component) for (a) 6 h (06/18) along axis A-A' (Fig. 2a), (b) 12 h (07/00) along axis A-A', and (c) 18 h (07/06) along axis B-B'. The isotach interval is 2 m s^{-1}. Tick marks are plotted along the abscissa every 50 km.

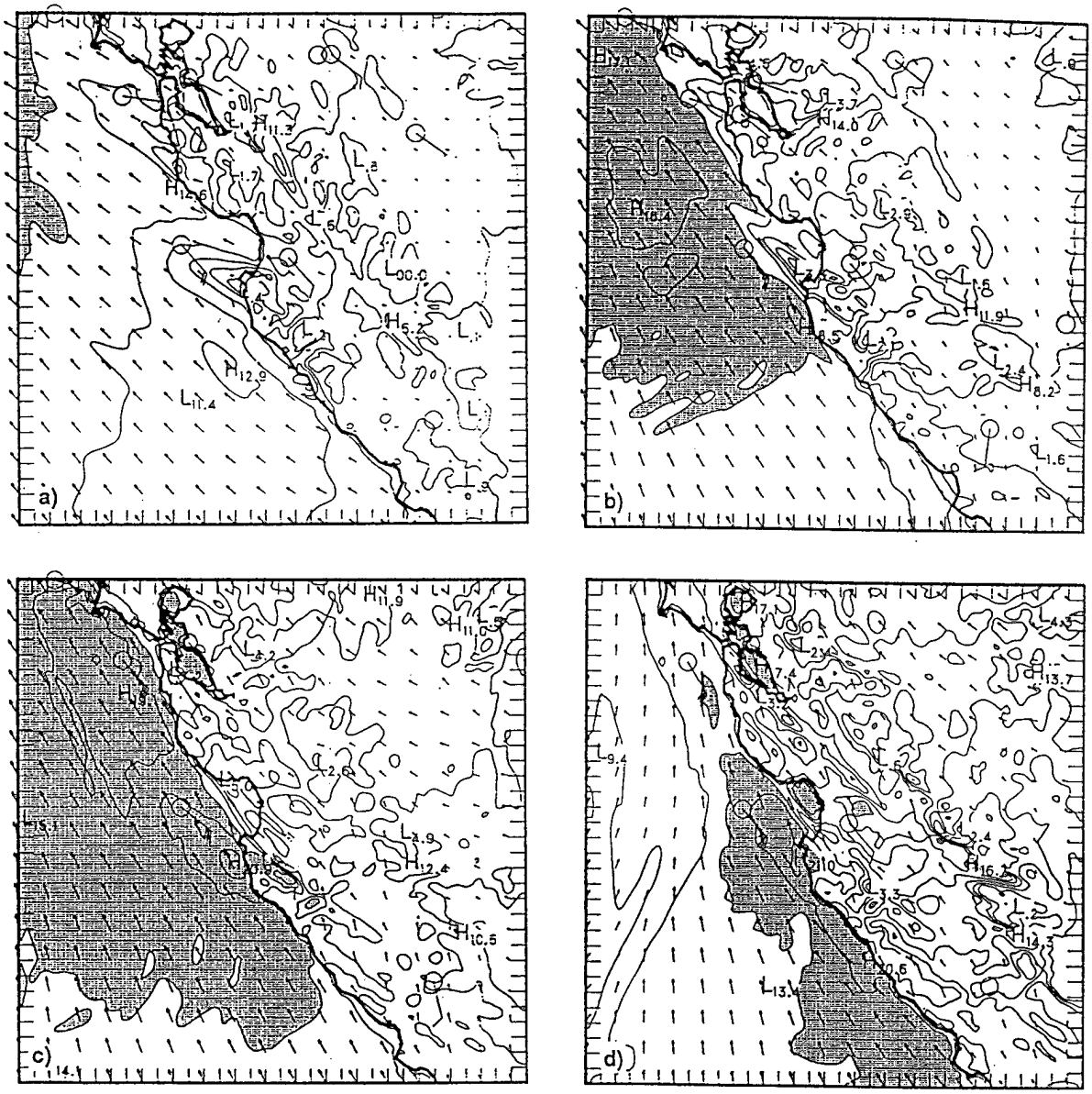

Fig. 12. Model-simulated 5-m wind speed and direction for the inner grid-mesh domain (Δx=2 km) for (a) 6 h (06/18), (b) 9 h (06/21), (c) 12 h (07/00), and (d) 15 h (07/03). The isotach interval is 2.5 m s^{-1}. Wind speeds greater than 15 m s^{-1} are shaded. Model-simulated wind speed and direction are shown by the vectors plotted every 10 grid points. Surface wind observations of interest are represented by the wind barbs, with one full barb equivalent to 5 m s^{-1}. The tick mark interval is 10 km or 5 grid points.

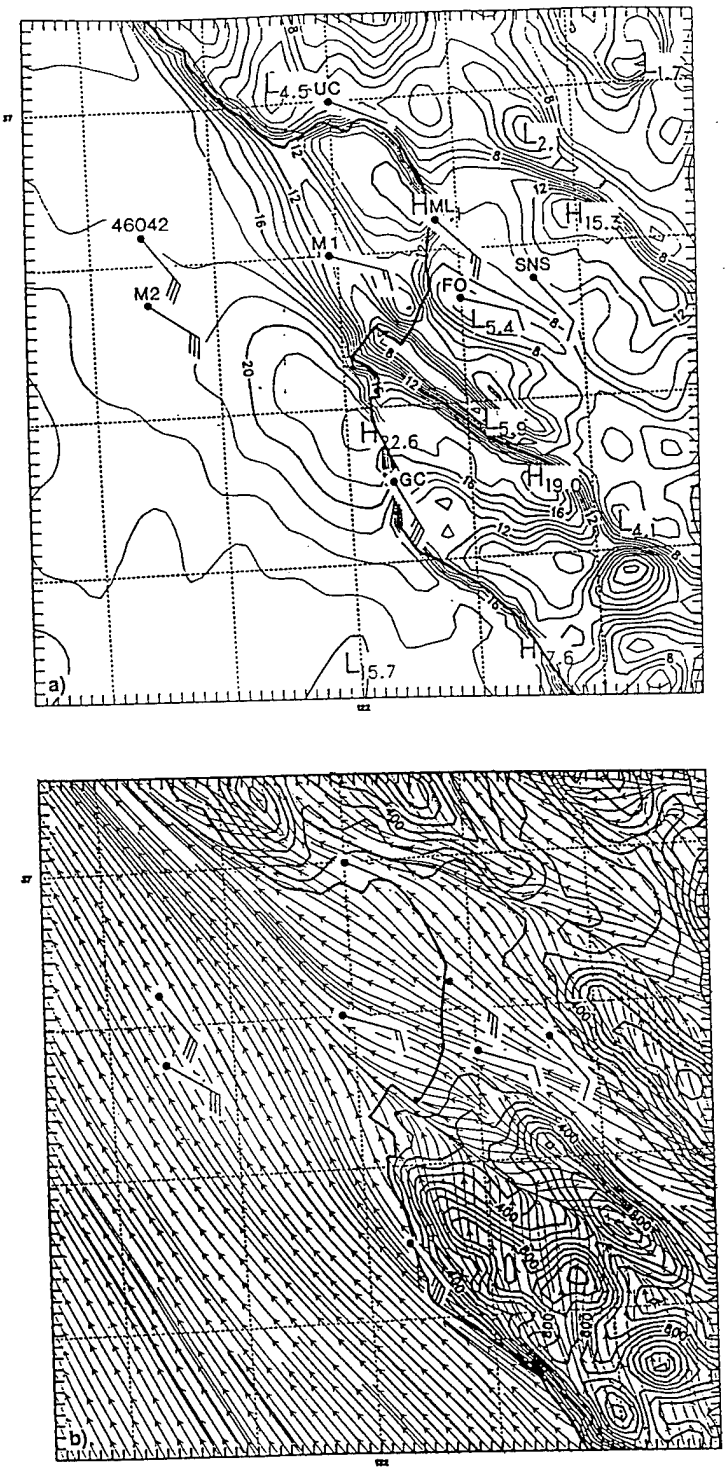

Fig. 13. Subsection of the model inner grid-mesh domain (Δx=2 km) of the 13-h simulated (a) 5-m wind speed and (b) 5-m streamlines. The isotach interval in (a) is 1 m s^{-1}. Model terrain height is plotted every 100 m in (b). Surface wind observations are represented by the wind barbs, with one full barb equivalent to 5 m s^{-1}. Station observation identifications are plotted in (a). Tick marks are plotted around the border every grid point or 2 km.

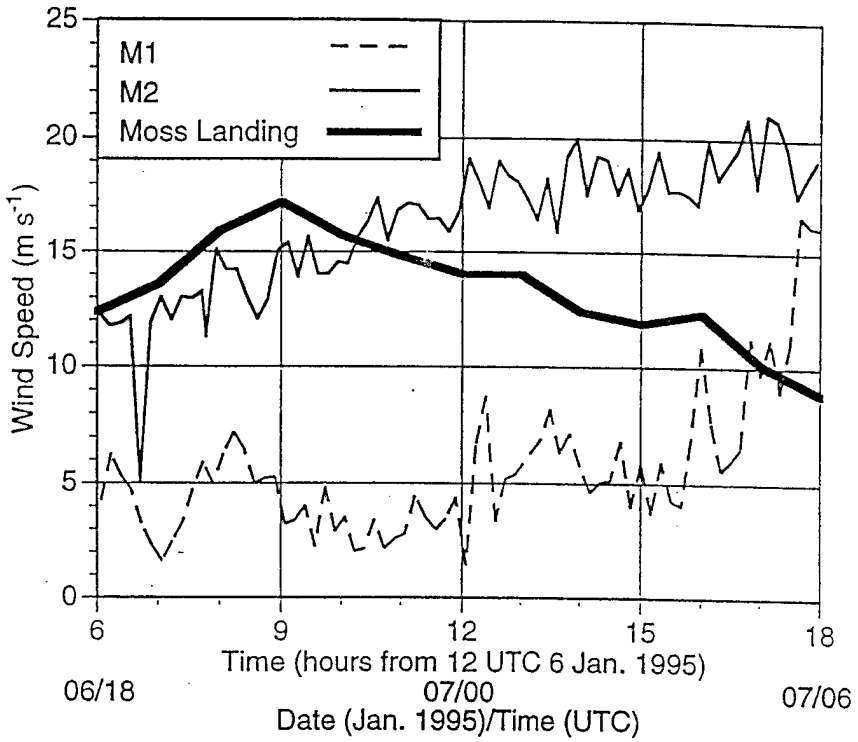

Fig. 14. Time series between 06/18 and 07/06 of observed surface wind speed for buoy M1 (dashed), buoy M2 (thin solid), and Moss Landing (ML, heavy solid).

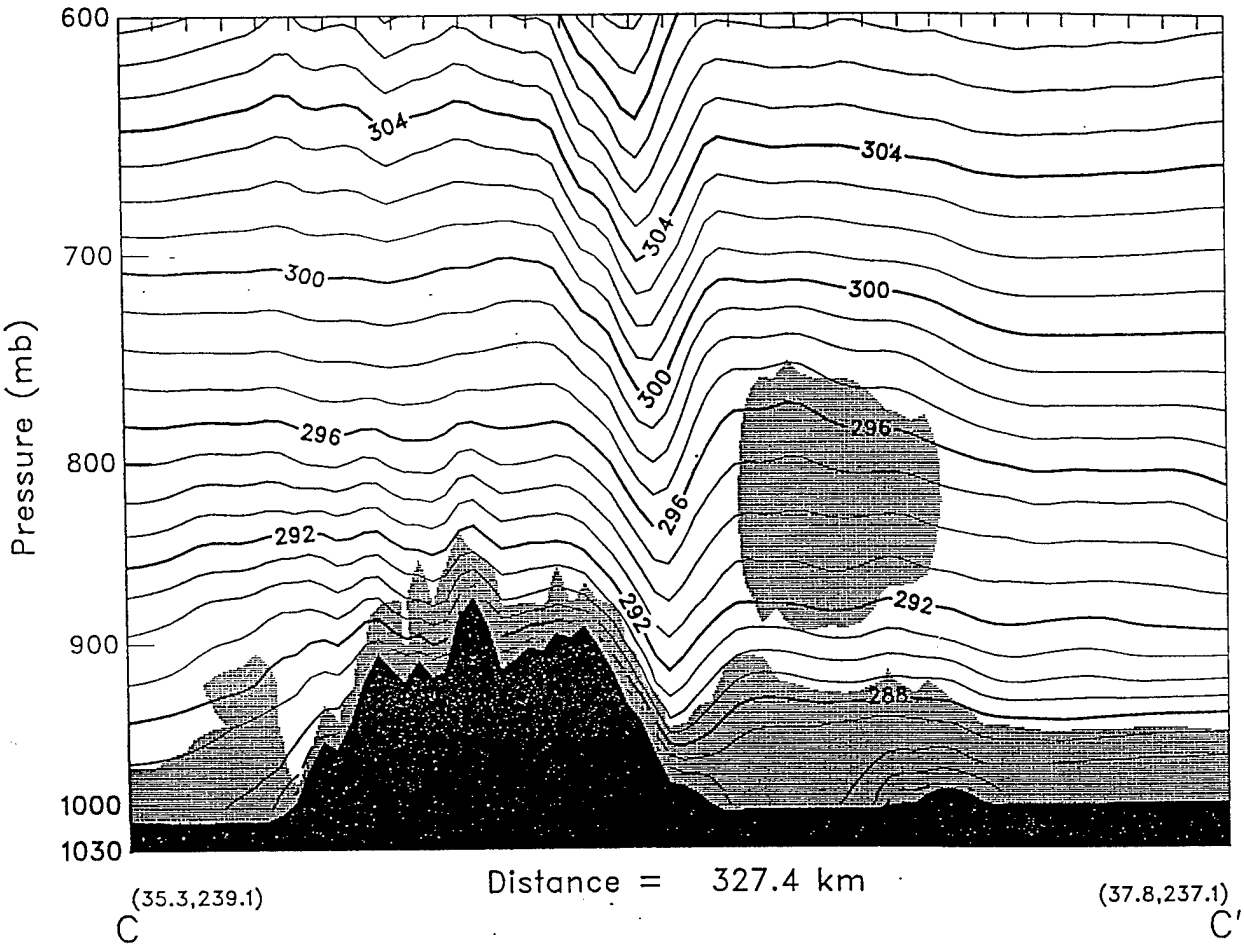

Fig. 15. Vertical cross section along axis C-C' (see Fig. 2b) of model-simulated potential temperature (K) for the 13-h simulation time (07/01). The isentrope interval is 1 K. Turbulent kinetic energy greater than 0.5 $m^2 s^{-2}$ is shaded. Tick marks are plotted along the abscissa every 10 km.

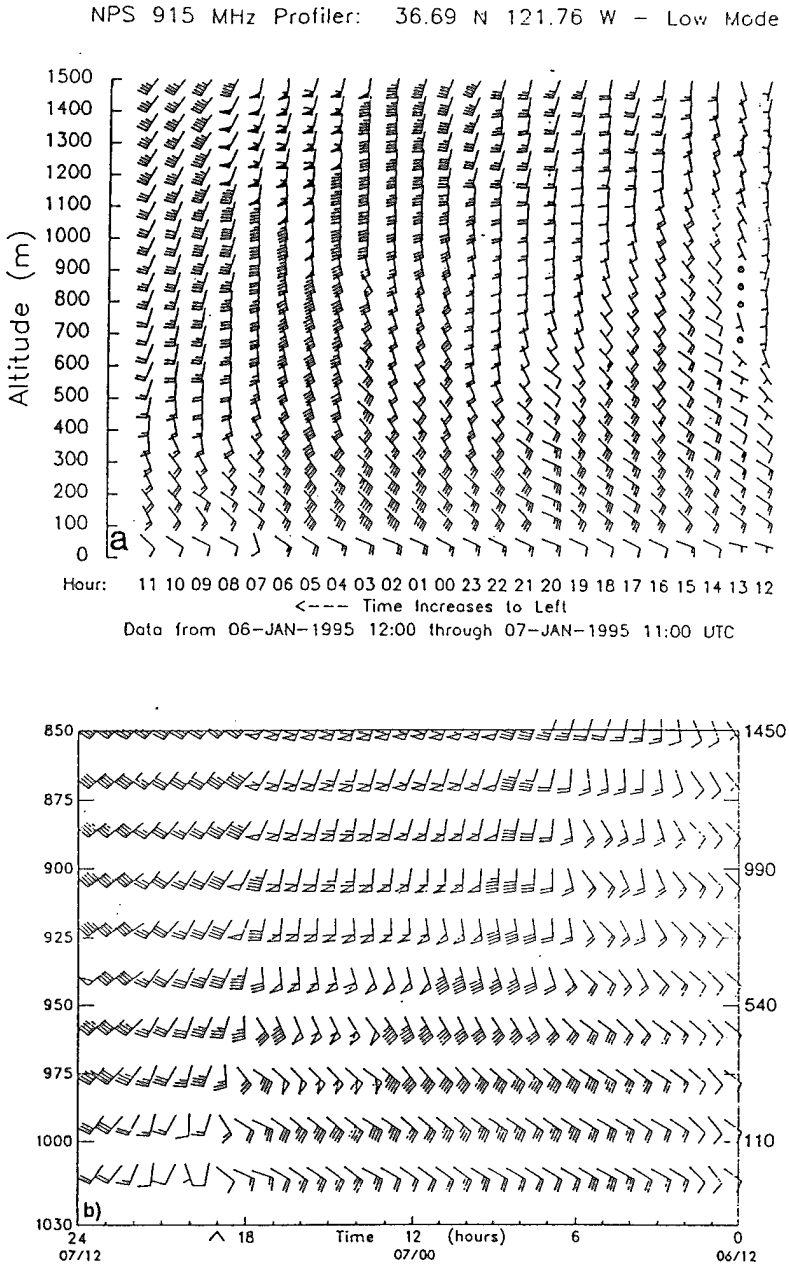

Fig. 16. Wind speed and direction displayed as (a) time-height section of hourly observations between 06/12 and 07/11 from the Naval Postgraduate School's 915 MHz wind profiler located at Fort Ord (location FO in Fig. 6a) and (b) time-pressure section between 0 h (06/12) and 24 h (07/12) of model-simulated winds interpolated to the Fort Ord site. Geopotential heights for a standard atmosphere are shown in (b). One full barb is equivalent to 5 m s^{-1} and a flag represents 25 m s^{-1}. Frontal passage is indicated by the caret in (b).

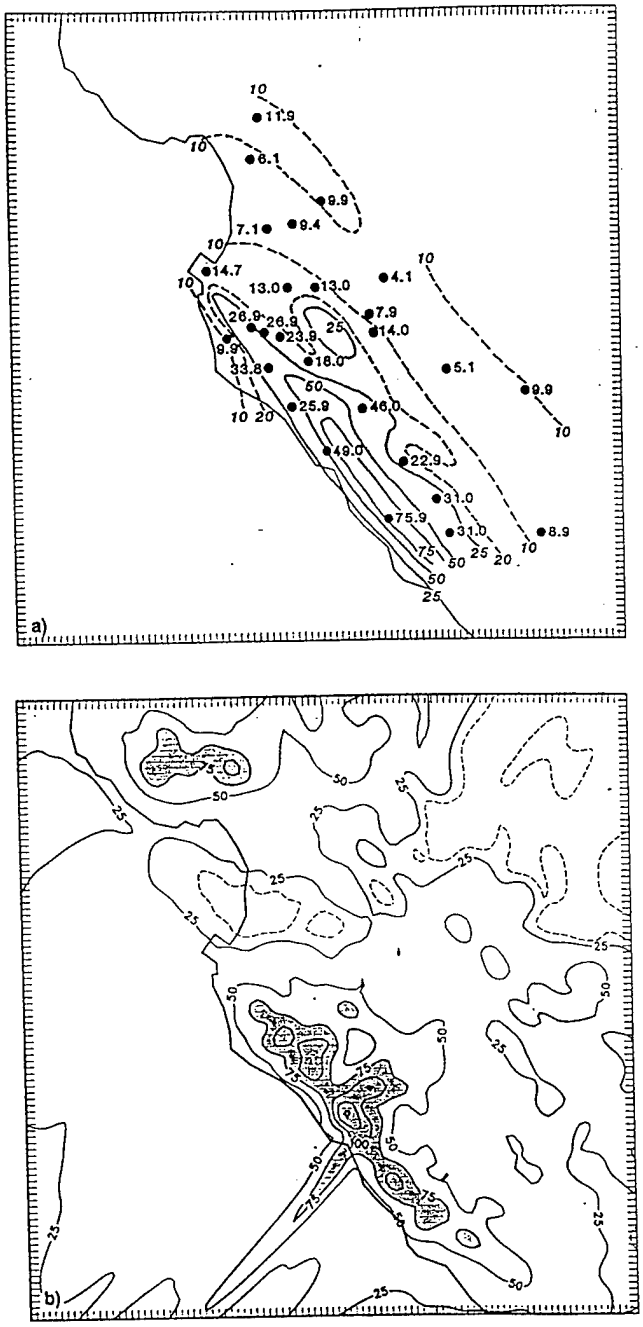

Fig. 17. The 24-h accumulated (a) observed precipitation analysis and (b) model-simulated precipitation between 06/12 and 07/12. The isohyet interval is 25 mm. The 10 and 20 mm isohyets are shown as dashed isopleths. Station observations are plotted in mm in (a). Precipitation in excess of 75 mm is shaded in (b). Only a portion of the inner-compuational mesh is shown in (b).

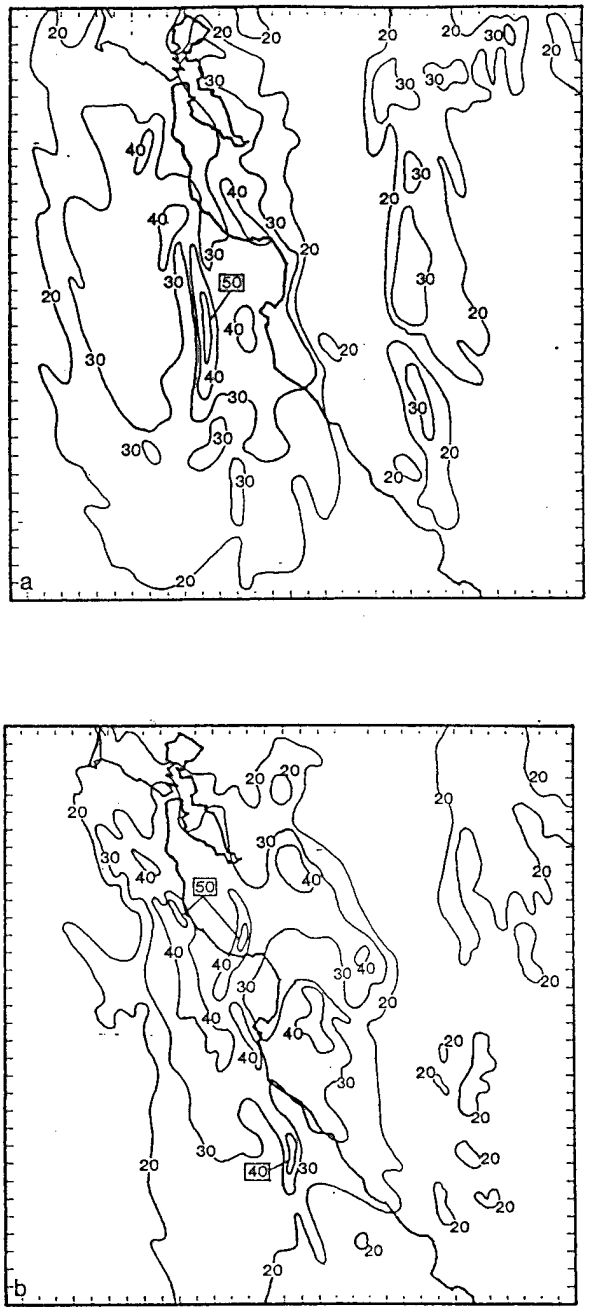

Fig. 18. Radar reflectivity (dBZ) from the National Weather Service WSR-88D Doppler radar data for (a) 0600 UTC 7 January and (b) 0653 UTC 7 January. The isopleth interval is 10 dBZ beginning with 20 dBZ.

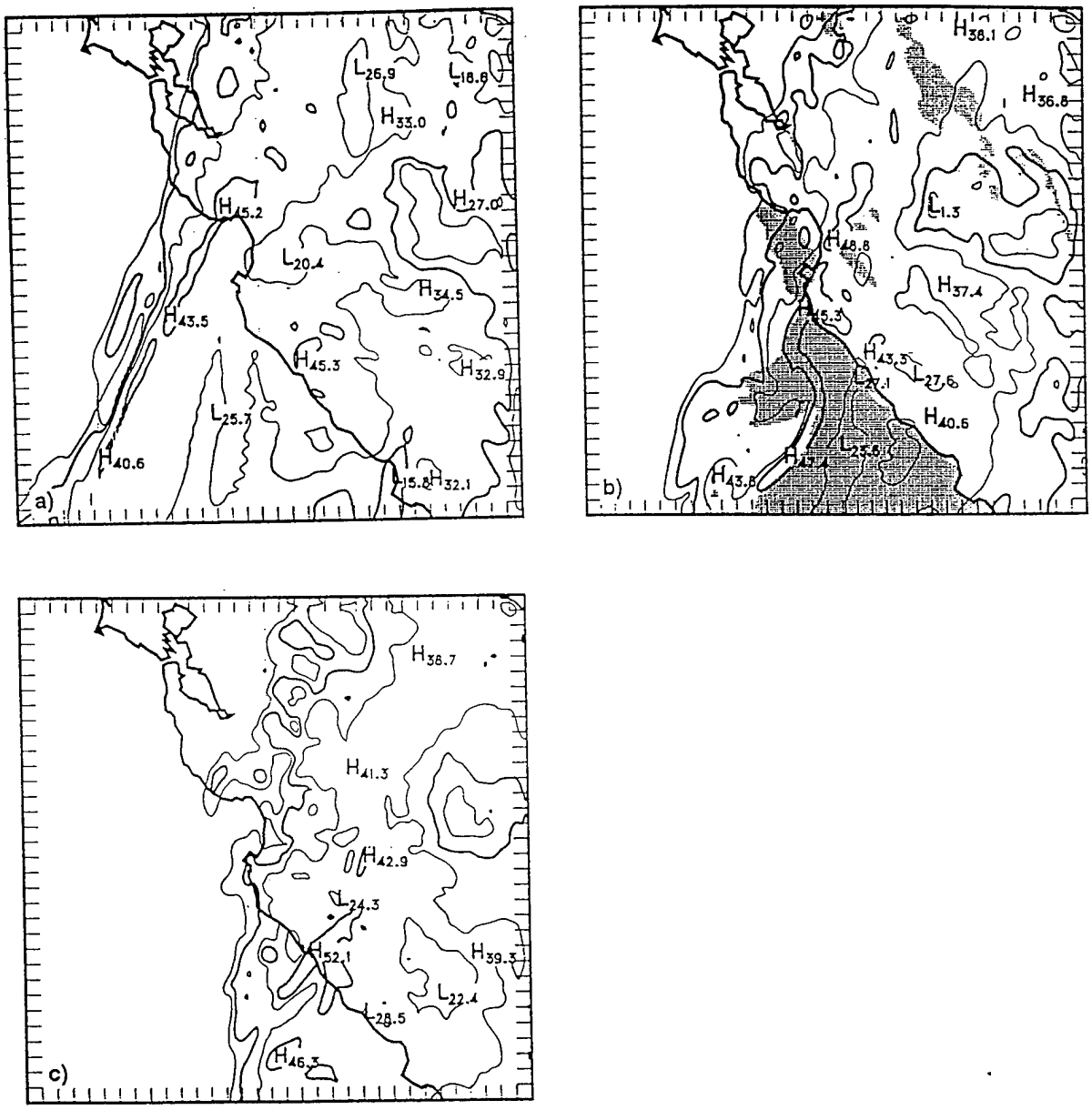

Fig. 19. Model-simulated 900-mb radar reflectivity (dBZ) for the (a) 16-h time (0400 UTC 7 January), (b) 17.3 h time (0520 UTC 7 January), and (c) 18.7 h time (0640 UTC 7 January). The isopleth interval is 10 dBZ. The 975-mb wind speed in excess of 30 m s^{-1} is shaded in (b).

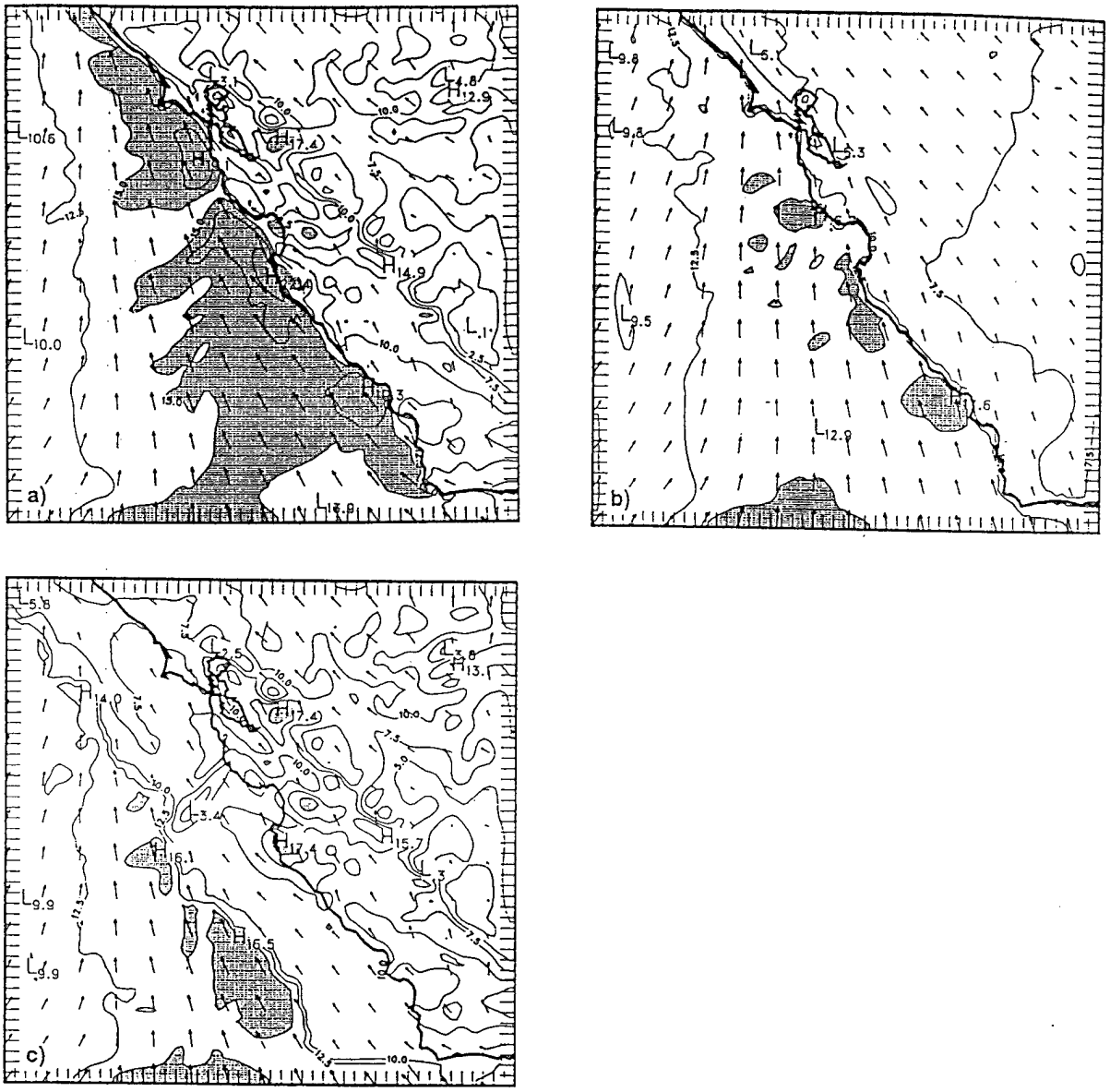

Fig. 20. Model-simulated 5-m wind speed and direction for the inner grid-mesh domain (Δx=5 km) for the 15-h simulation time (07/03) for (a) CTRL, (b) NOTOPO, and (c) COAST. The isotach interval is 2.5 m s^{-1}. Wind speeds greater than 15 m s^{-1} are shaded. Model-simulated wind speed and direction are shown by the vectors plotted every 7 grid points. The tick mark interval is 10 km or 2 grid points.

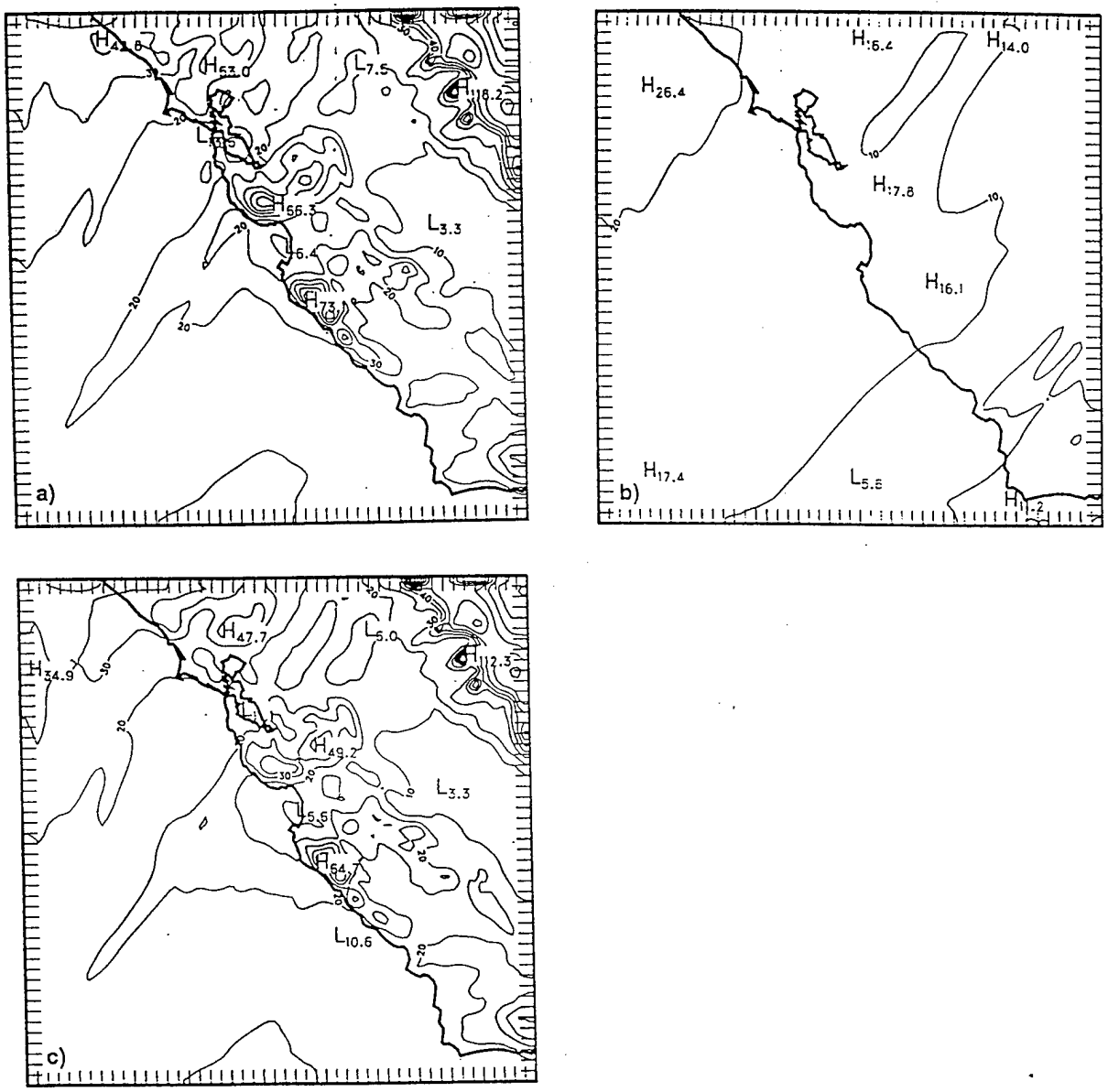

Fig. 21. Model-simulated 24-h accumulated precipitation valid at 07/12 for the inner grid-mesh domain (Δx=5 km) for (a) CTRL, (b) NOTOPO, and (c) COAST. The contour interval is 10 mm.

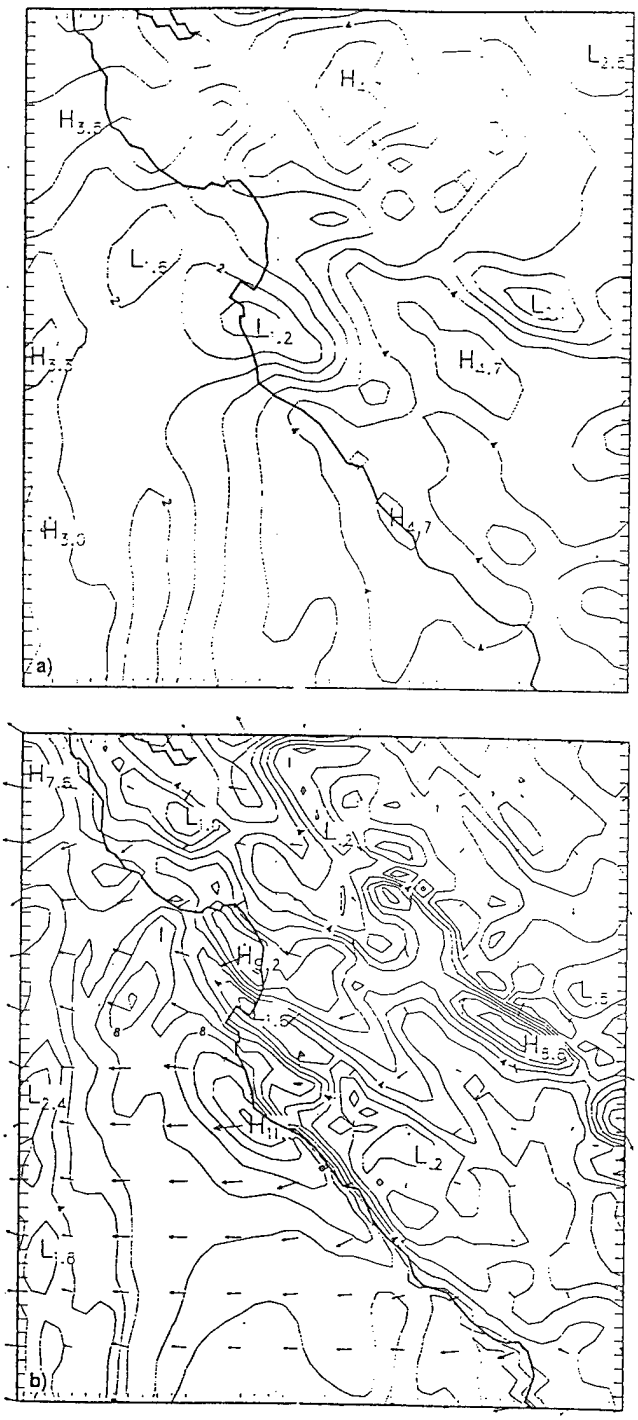

Fig. 22. The 15 h (07/03) (a) sea-level pressure perturbation (difference field CTRL minus NOTOPO) and (b) 5-m wind velocity perturbation (difference field CTRL minus NOTOPO) for a portion of the inner mesh (Δx=2 km). The isobar interval in (a) is 0.5 mb and the isotach interval in (b) is 1 m s^{-1}.

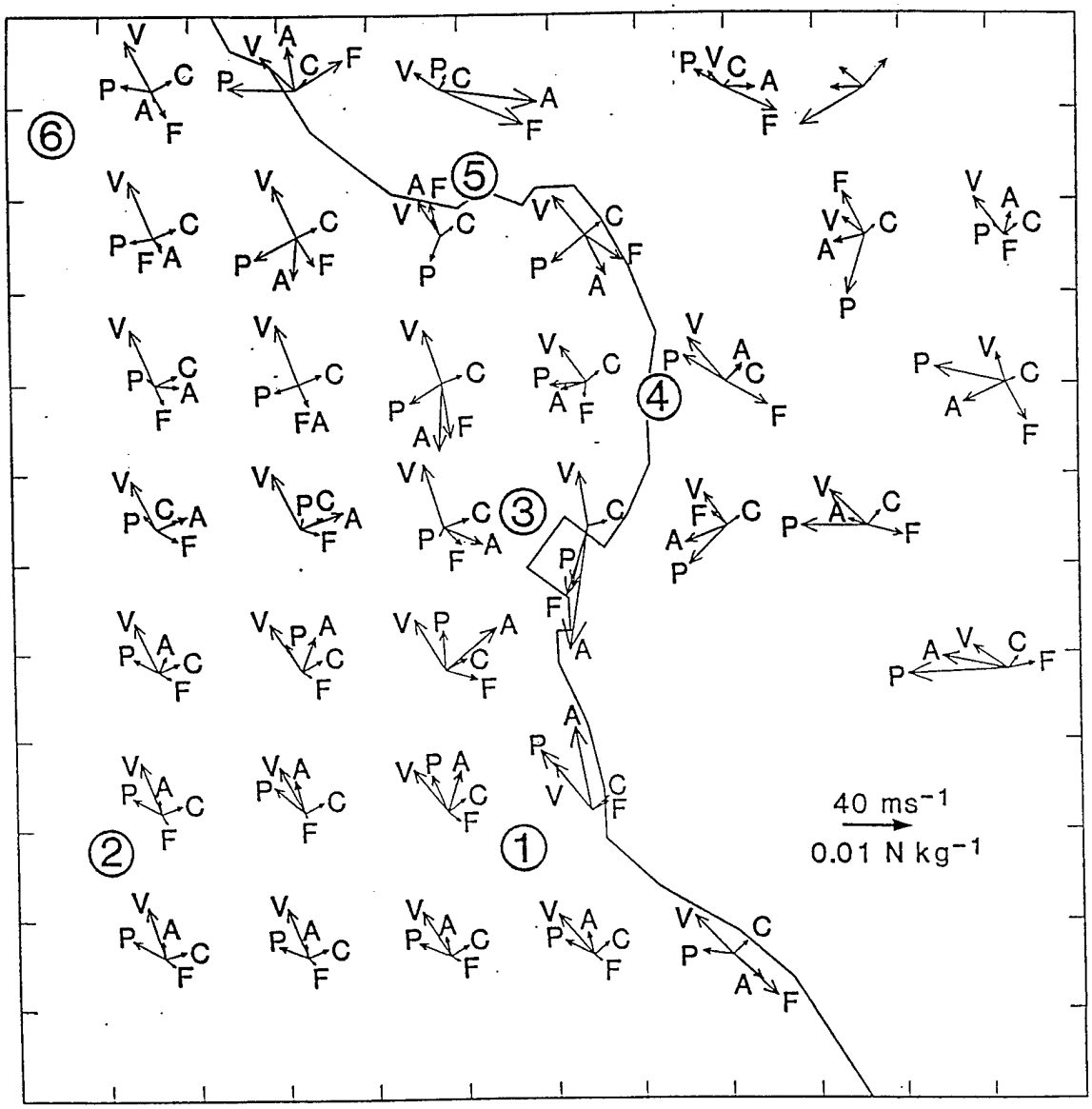

Fig. 23. Vector representation of momentum-budget terms at 975 mb valid at the 14-h simulation time (07/02) for a portion of the inner mesh (Δx=2 km). The velocity, pressure gradient force, Coriolis force, and parcel acceleration are labeled **V**, **P**, **C**, and **A**, respectively. The friction or residual vector is labeled by **F**.

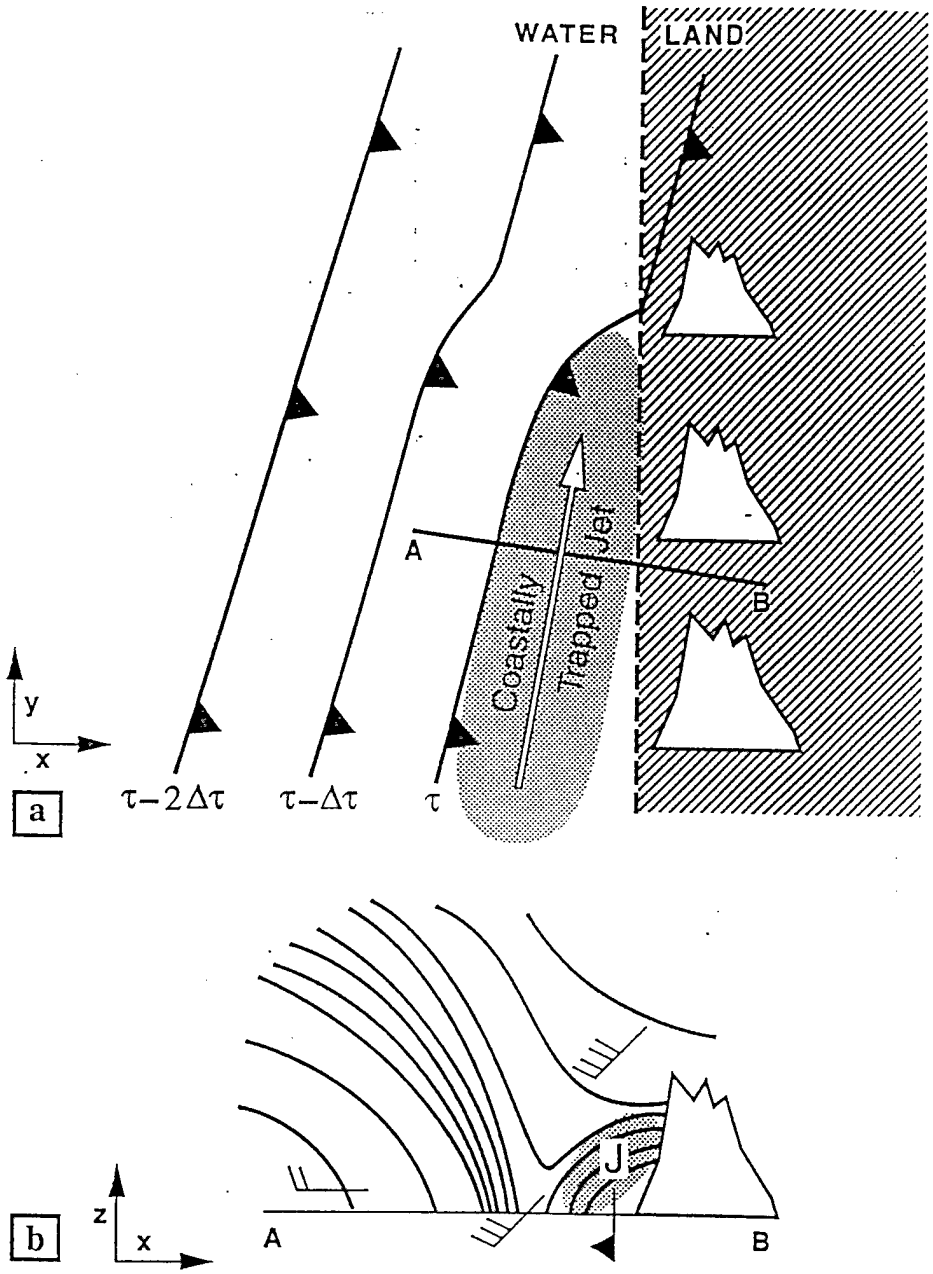

Fig. 24. Schematic diagram showing the evolution of a surface frontal system as it impinges upon coastal topography (a). The land surface is shown by the hatched region. The coastally trapped jet is shaded. A schematic vertical cross section of potential temperature through the front and coastal jet (along axis AB). The coastal jet is shaded with schematic wind barbs as shown.